The RNA splicing factor PRPF8 is required for left-right organiser cilia differentiation and determination of cardiac left-right asymmetry via regulation of *Arl13b* splicing

Fangfei Jiang[1]†, Michael Boylan[1]†, Dale W. Maxwell[1,2]†, Wasay Mohiuddin Shaikh Qureshi[1], Charlie F. Rowlands[1], Gennadiy Tenin[1,9], Karen Mitchell[1], Louise A. Stephen[1], Elton J. R. Vasconcelos[3], Dapeng Wang[3], Tong Chen[4], Junzhe Zha[5], Jingshu Liu[1], Nouf Althali[1,6], Dragos V. Leordean[1], Meurig T. Gallagher[7], Basudha Basu[8], Katarzyna Szymanska[8], Advait Veeraghanta[2], Bernard Keavney[9-11], Martin J. Humphries[5], Jamie Ellingford[1,12], David Smith[7], Colin A. Johnson[8], Raymond T. O'Keefe[1], Sudipto Roy[2,13], Kathryn E. Hentges[1]*

Author Affiliations:

1. Division of Evolution, Infection and Genomics, BHF Manchester Centre of Research Excellence, School of Biological Sciences, Faculty of Biology, Medicine, and Health, Manchester Academic Health Science Centre, University of Manchester, Manchester, M13 9PT, UK

2. Institute of Molecular and Cell Biology (IMCB), Agency for Science, Technology and Research (A*STAR), Proteos, 61 Biopolis Drive, Singapore 138673, Singapore

3. LeedsOmics, University of Leeds, Leeds, LS2 9JT, UK

4. Division of Molecular and Cellular Function, School of Biological Sciences, Faculty of Biology, Medicine, and Health, Manchester Academic Health Science Centre, University of Manchester, Manchester, M13 9PT, UK

5. Division of Cell Matrix Biology and Regenerative Medicine, Manchester Cell-Matrix Centre, School of Biological Sciences, Faculty of Biology, Medicine, and Health, Manchester Academic Health Science Centre, University of Manchester, Manchester, M13 9PT, UK

6. Biology Department, Science College, King Khalid University, Abha, Saudi Arabia.

7. Centre for Systems Modelling and Quantitative Biomedicine, University of Birmingham, Edgbaston, Birmingham, UK and Centre for Human Reproductive Science, University of Birmingham, Birmingham, UK

8. Division of Molecular Medicine, Leeds Institute of Medical Research, University of Leeds, Leeds, LS9 7TF, UK

9. Division of Cardiovascular Sciences, BHF Manchester Centre of Research Excellence, School of Medical Sciences, Faculty of Biology, Medicine, and Health, The University of Manchester, Manchester, M13 9PL, UK

10. Manchester Heart Centre, Manchester University NHS Foundation Trust, Manchester Academic Health Science Centre, UK

11. NIHR Manchester Biomedical Research Centre, UK

112. Genomics England, London, E14 4AB, UK

13. Department of Paediatrics, National University of Singapore, 1E Kent Ridge Road, Singapore 119228, Singapore

† = equal contribution
*= author for correspondence, Tel +44 161 275 1490, email:
Kathryn.hentges@manchester.ac.uk

Short title: PRPF8 mutation alters cilia function and organ laterality

Present addresses are listed in supplemental table 6.

Abstract

Cilia function in the left-right organizer (LRO) is critical for determining internal organ asymmetry in vertebrates. To further understand the genetics of left-right asymmetry, we isolated a mouse mutant with laterality defects, *l11Jus27,* from a random mutagenesis screen. *l11Jus27* mutants carry a missense mutation in the pre-mRNA processing factor, *Prpf8*. *cephalophŏnus (cph)* mutant zebrafish, carrying a protein truncating mutation in *prpf8*, phenocopy the laterality defects of *l11Jus27* mutants. *Prpf8* mutant mouse and fish embryos have increased expression of an alternative transcript encoding the cilium-associated protein, ARL13B, that lacks exon 9. In zebrafish, over-expression of the *arl13b* transcript lacking exon 9 perturbed cilium formation and caused laterality defects. The shorter ARL13B protein isoform lacked interactions with intraflagellar transport proteins. Our data suggest that PRPF8 plays a prominent role in LRO cilia by through the regulation of alternative splicing of ARL13B, thus uncovering a new mechanism for cilia-linked developmental defects.

Key words:

PRPF8, cilia; left-right axis, splicing, IFT, ARL13B, mutagenesis screen, ciliopathy, retinitis pigmentosa, embryonic development

86 **Introduction**

87 Cilia are specialised hair-like organelles required for many cellular functions (1). Motile cilia
88 produce a rhythmic waving or beating motion, whereas non-motile cilia act as sensory antennae
89 for cells (1, 2). Diseases caused by cilia dysfunction are collectively known as ciliopathies.
90 Mutations in the wide range of genes required for cilia function cause ciliopathies, with most
91 phenotypes displaying both genetic heterogeneity and variable expressivity (3). In humans,
92 mutations in several spliceosomal pre-mRNA processing factor proteins cause autosomal
93 dominant Retinitis Pigmentosa (RP) (4-6), a ciliopathy causing progressive retinal atrophy and
94 loss of sight with age. RP-causing mutations in Pre-mRNA Processing Factor 8 (PRPF8)
95 produce multiple splicing defects (5, 7-11). However, PRPF8 may have a more direct role in
96 cilia functionality. PRPF8 localises to the basal body of primary cilia, and knocking down
97 PRPF8 in human and mouse cells (12, 13), zebrafish embryos (13) and *C. elegans* (14), inhibits
98 ciliogenesis.

99

100 In vertebrate embryogenesis, specialised motile cilia in the LRO play a critical role in left-right
101 axis specification (2, 15). In mice, laterality is established at the ventral node (2), the
102 mammalian LRO. The node is a teardrop shaped pit at the posterior end of the notochord with
103 motile cilia; these cilia generate a leftward flow of fluid within the node cavity thought to be
104 detected by immotile cilia on adjacent perinodal 'crown' cells (16-20). In response, expression
105 of the genes *Cerl2* and *Nodal*, becomes restricted preferentially on the right and left side of the
106 node, respectively (21-23). Nodal in the left lateral plate mesoderm (LPM) induces expression
107 of the Nodal inhibitors *Lefty1* and *Lefty2* (24, 25) at the midline and left LPM, respectively
108 (26). Nodal in the LPM also induces expression of the transcription factor *Pitx2* (27). *Pitx2* is
109 considered to be the effector of Nodal signalling, and is required for the correct positioning and

110 morphogenesis of organs including the heart, lungs, gut and blood vessels (28-30), but is
111 dispensable for heart looping directionality (reviewed in (31)) .
112
113 A recessive lethal mouse mutant with laterality defects was isolated from a random chemical
114 mutagenesis screen: the *l11Jus27* mouse (32, 33). The causative mutation in this mouse is an
115 asparagine (N) to serine (S) missense mutation at residue 1531 in *Prpf8*, the mouse orthologue
116 of human *PRPF8*. *Prpf8*$^{N1531S/N1531S}$ embryos (hereafter referred to as *Prpf8*^{N1531S} mutants or
117 *Prpf8*^{N1531S} hom) have impaired LRO cilia formation and motility. Zebrafish *cph* mutants
118 (carrying a Prpf8 truncation mutation) phenocopy laterality defects seen in *Prpf8*^{N1531S} mutant
119 mouse embryos. Moreover, modelling the analogous *Prpf8*^{N1531S} mutation in yeast resulted in
120 splicing defects. Bulk RNA-seq analysis of *Prpf8*^{N1531S} mutant mouse embryos showed
121 increased skipping of exon 9 in the transcript of the Arf-like GTPase *Arl13b;* the ARL13B
122 protein is specifically localised to the ciliary membrane (34, 35) where it functions in regulating
123 cilia length, and thus impacts upon beat pattern and flow (36-38), as well as ciliary trafficking
124 via interactions with intraflagellar transport (IFT) proteins (39, 40). Importantly, over-
125 expression of the shorter a*rl13b* transcript (lacking exon 9) in wild type zebrafish re-capitulated
126 many aspects of the *Prpf8*^{N1531S} mutant phenotype. Additionally, the ARL13B protein lacking
127 the region encoded by exon 9 showed reduced binding to IFT partners. Combined, these results
128 suggest that altering *Arl13b* alternative transcript ratios may be the mechanistic basis for the
129 laterality defects observed in *Prpf8* mutants. The data presented here reveal specific functions
130 for PRPF8 in cilia function and embryonic patterning, which may also provide new insights
131 into the role of PRPF8 in disease pathology in patients with RP.

132 **Results**

133 **Phenotypic analysis of *l11Jus27* mouse mutants**

134 The *l11Jus27* mouse line was isolated from a random chemical mutagenesis screen, which
135 employed a balancer chromosome to facilitate mapping of mutations (32). *l11Jus27*
136 heterozygotes are viable and fertile. At E8.25, *l11Jus27* homozygous embryos appear grossly
137 normal (Supplemental Fig. 1a-b) but are developmentally delayed (Supplemental Fig. 1c). At
138 E9.5 the *l11Jus27* homozygotes have an open neural tube, distended heart tube, and a high
139 incidence of reversed cardiac looping (Fig. 1a). At E10.5 less severely affected mutants have
140 milder cardiac defects and developmental delay (Supplemental Fig. 1d-f). More severely
141 delayed embryos have also failed to undergo chorioallantoic fusion (Supplemental Fig. 1f).
142 *l11Jus27* homozygous embryos have impaired yolk sac vascularisation at E9.5 (Supplemental
143 Fig. 1g-h) and frequently do not have patent umbilical vessels (Supplemental Fig 1i-j),
144 probably leading to the failure in chorioallantoic fusion observed in mutant embryos at E10.5
145 (Supplemental Fig 1j; penetrance reported in Supplemental Table 1). The majority of
146 homozygous mutant embryos died by E11.5, and none were isolated after E12.5.

147

148 **The *l11Jus27* line contains a *Prpf8*^{N1531S} mutation**

149 The *l11Jus27* mutant mouse line was isolated from a balancer chromosome mutagenesis
150 screen; therefore the causative mutation was known to reside in a 24cM region of mouse
151 chromosome 11 (32). Meiotic mapping further refined the *l11Jus27* candidate interval
152 (Supplemental Fig. 1k) (41). Genome sequencing of an E10.5 homozygous mutant embryo
153 revealed a novel point mutation of an A to G transition within the genetic candidate interval at
154 position chr11: 75,391,978 (mm39), which produces a N1531S missense mutation in *Prpf8*.
155 This sequence alteration was confirmed in an additional 3 homozygous mutant embryos and
156 was not present in wild type C57BL/6 or 129S5 animals (Fig. 1b). Thus, we concluded the

157 *l11Jus27* line carries a PRPF8 N1531S missense mutation, and *l11Jus27* homozygous embryos
158 will now be referred to as *Prpf8* hom. We confirmed by quantitative RT-PCR that the N1531S
159 mutation does not affect *Prpf8* transcript levels (Fig. 1c). PRPF8 is highly conserved (42), and
160 residue N1531 is conserved between multiple eukaryotes (Fig. 1d). The N1531S amino acid
161 substitution is in a linker region near the endonuclease-like domain (Fig. 1e; (43)) and is
162 predicted to be damaging by PolyPhen and SIFT (44, 45) in both mouse and human proteins.
163 At E10.5, mutants appeared to display a reduction in PRPF8 protein levels, but this was not
164 significantly different (Fig. 1f-g; one-way ANOVA p=0.4212)(12). To test if the PRPF8
165 mutation altered protein stability, we expressed an N-terminal FLAG epitope-tagged PRPF8
166 construct in mammalian cells (Fig. 1h) and performed a cycloheximide assay to determine the
167 PRPF8 degradation rate. We detected a reduced level of epitope tagged PRPF8^{N1531S} protein
168 compared to wild type protein at each time point in the assay, but the overall degradation rate
169 of the N1531S mutant was similar to the wild type construct (Wilcoxon test p=0.125; Fig. 1i-
170 j), and thus did not indicate significant evidence of increased protein degradation.
171

172 **Nodal cilia are present but dysmotile in *Prpf8*^{N1531S} mutants**

173 Heart looping defects are associated with ciliopathies (46, 47). Scanning electron microscopy
174 (SEM) revealed that control and *Prpf8*^{N1531S} mutant embryos possessed abundant nodal cilia at
175 the 2-3 somite stage (Fig. 2a-d). Control embryos had stereotypical pit shaped nodes (Fig. 2a,
176 n=7), whereas *Prpf8*^{N1531S} mutant embryonic nodes appeared unusually flat (Fig. 2b, *n*=6/8),
177 suggesting that node morphogenesis is disrupted in *Prpf8*^{N1531S} mutant embryos. While there
178 was a trend towards fewer cilia in *Prpf8*^{N1531S} mutant embryos, this trend was not statistically
179 significant (Fig. 2e; unpaired t-test of late head fold (LHF) stage data, p=0.1934; for 2-3 somite
180 data p=0.1494). Transmission electron microscopy (TEM) analysis of nodal cilia did not reveal
181 any overt differences between homozygous *Prpf8*^{N1531S} mutant embryos and controls

182 (Supplemental Fig 2). Because mutations in the spliceosome have been found to affect the rate
183 of cell division (48), we performed immunofluorescence staining for phospho-histone H3 to
184 identify cells in mitosis. There was no difference in the percentage of dividing cells between
185 genotypes (Fig. 2f; unpaired t-test p=0.7918). Using acetylated tubulin as a marker of cilia (Fig.
186 2g-h), we found that node cilia length in homozygous *Prpf8*^{N1531S} mutant embryos was
187 significantly shorter than in heterozygous control embryos (Fig. 2i, unpaired t-test p=0.0408).
188
189 LRO fluid flow generation is related to cilia length (38). Therefore, we evaluated whether flow
190 was established correctly in *Prpf8*^{N1531S} mutant embryo nodes. We placed microbeads in the
191 node of embryos mounted in a chamber slide to detect the direction of nodal flow. While almost
192 all heterozygotes established flow towards the left of the node (*n*=5/6; Fig. 2j; Supplemental
193 Movie File 1), almost all *Prpf8*^{N1531S} mutants failed to establish any directional fluid flow
194 (*n*=5/6; Fig. 2k); instead the microbeads showed random Brownian motion (Supplemental
195 Movie file 2). We next investigated whether cilia motility was impaired in mutant embryos.
196 Directly visualising cilia movement using high-speed videomicroscopy revealed that wild type
197 embryos had strongly beating cilia (*n*=5 Supplemental Movie File 3), as did *Prpf8*$^{N1531S/+}$
198 embryos (*n*=4/4). However, *Prpf8*^{N1531S} homozygotes had very few motile cilia (*n*=3;
199 Supplemental Movie File 4). We quantified the number of motile cilia (Fig. 2l) and found
200 significant differences between the three genotypes (p=0.0058, Welch's ANOVA). Posthoc
201 testing revealed that the number of motile cilia in *Prpf8*^{N1531S} homozygotes was significantly
202 lower compared to *Prpf8*$^{+/+}$ (p=0.0222) and *Prpf8*$^{N1531S/+}$ embryos (p=0.0487), but not between
203 *Prpf8*$^{N1531S/+}$ and *Prpf8*$^{+/+}$ embryos.
204
205

206 PRPF8 has been reported to localise to the base of cilia (12-14). To determine if the *Prpf8*^{N1531S}
207 missense mutation affected protein localisation, we used immunofluorescence to analyse node
208 cilia. We confirmed that PRPF8 protein can be detected at the base of some cilia in
209 heterozygous (Supplemental Fig. 3 a-c) and *Prpf8*^{N1531S} homozygous mutant embryos within
210 the node (Supplemental Fig. 3 g-i). A transverse projection of the Z-stack of confocal images
211 confirmed that the node in heterozygous embryos formed a pit like structure (Supplemental 3d-
212 f) but in homozygotes the node was flatter (Supplemental 3 j-l). These findings suggest that
213 *Prpf8*^{N1531S} homozygous mutants have defects in node structure, cilia motility, and nodal fluid
214 flow that are consistent with downstream defects in L-R axis formation.
215
216 **Laterality gene expression analysis reveals pathway defects in *Prpf8*^{N1531S} mutants**
217 We next determined whether the L-R axis pathway was disturbed by the defects in the node.
218 We performed whole-mount *in situ* hybridisation for several genes that are important for L-R
219 axis formation and found that *Prpf8*^{N1531S} mutant embryos had highly aberrant laterality gene
220 expression patterns. *Shh*, needed for L-R axis establishment (49), was expressed in the midline
221 and node of both control and *Prpf8*^{N1531S} mutant embryos (Fig. 3a-b), though half of *Prpf8*^{N1531S}
222 mutants displayed fainter and discontinuous midline *Shh* expression (*n*=3/6) *Cerl2* (Fig. 3c-e)
223 and *Nodal* (Fig. 3f-h) expression was highly variable, with normal, reversed, symmetric and
224 absent expression patterns observed for both genes in the mutants. The LPM of *Prpf8*^{N1531S}
225 mutants usually lacked *Nodal* expression (*n*=19/21), and when *Nodal* was expressed, the
226 expression domain did not include the anterior LPM. Accordingly, both *Lefty1* and *Lefty2* were
227 not expressed in *Prpf8*^{N153S1} mutant embryos (*n*=10/10) (Fig 3i-j). *Pitx2* expression in the LPM
228 and subsequent secondary heart field (50), which is induced by Nodal activity, was variable,
229 with normal (n=13/38), reversed (n=8/38), bilateral (n=8/38) and absent (n=9/38) expression
230 in *Prpf8*^{N153S1} mutant embryos (Fig 3k-p). *Pitx2* is normally expressed on the same side as the

231 developing ventricle. We quantified both *Pitx2* expression sidedness and heart looping
232 direction in mutant embryos (Fig 3q). In embryos where the sidedness of *Pitx2* expression was
233 unambiguous, 29% (n=6/21) expressed *Pitx2* on the opposite side of the embryo from the
234 inflow tract of the heart (Fig 3r). These data led us to hypothesise that the *Prpf8*^{N1531S} mutants
235 with reversed cardiac looping exhibited heterotaxy rather than *situs inversus.* To test this
236 hypothesis, we examined the expression of *Barx1* in the developing stomach (51), which is
237 found left of the embryonic midline. Both control and mutant embryos, including those with
238 reversed cardiac looping (n=6), maintained *Barx1* expression left of the midline, (Fig 3s-t),
239 supporting the hypothesis that *Prpf8*^{N1531S} mutant embryos model heterotaxy, not *situs*
240 *inversus*. The early lethality of *Prpf8*^{N1531S} mutant embryos precluded examining the laterality
241 of other organ systems.
242
243 **Phenocopy of *Prpf8* ^{N1531S} laterality defects in *prpf8* mutant zebrafish**
244 To evaluate if laterality defects present in the *Prpf8*^{N1531S} mouse showed evolutionary
245 conservation, we examined the ENU mutant zebrafish strain, *cph* (52). This mutant line
246 carries an E396* substitution in Prpf8, predicting a severely truncated protein (52). Whereas
247 wild type (Fig. 4a) and heterozygous embryos are phenotypically normal, *cph* homozygous
248 mutant embryos displayed a curled down body axis and delayed heart looping (Fig. 4b). *cph*
249 homozygotes displayed randomised cardiac looping: 27% of *cph* mutants had correctly
250 looped, 42% unlooped, and 31% reversed looped hearts, compared to 97%, 1% and 2%,
251 respectively, for wild type fish (Fig. 4c).
252
253 Laterality gene expression was altered in *cph* homozygous mutant zebrafish in a manner
254 resembling *Prpf8*^{N1531S} mutant mouse embryos. Homozygous *cph* mutant embryos had absent
255 or mis-localised expression of *lefty2* (*lft2*) (Fig. 4d-f) and *southpaw* (*spaw*), a zebrafish *Nodal*

256 homologue (Fig. 4g-i). Additionally, *dand5,* the zebrafish *Cerl2* homologue, which is
257 normally expressed more prominently on the right side of the embryo (Fig. 4j), displayed
258 altered expression patterns in *cph* embryos (Fig. 4k-l). The range of abnormal expression
259 patterns amongst mutant embryos for these key laterality genes is reminiscent of expression
260 defects found in *Prpf8*^{N1531S} mouse mutants. Overall, expression defects and heart looping
261 abnormalities found in *cph* zebrafish suggest that the role of PRPF8 in laterality
262 establishment and heart looping is conserved amongst vertebrates.
263
264 We next evaluated cilia formation and function in Kupffer's vesicle (KV), the zebrafish LRO.
265 Within KVs of wild type and *cph* zebrafish, motile cilia were present (Fig 4m), and no
266 significant reduction in overall number of cilia was found in mutants compared to wild type
267 controls (Fig 4n). However, there was a significant reduction in cilia length in *cph* mutants
268 relative to wild type controls (Fig 4o; unpaired t-test. $P<0.0001$), similar to our findings in
269 *Prpf8*^{N1531S} mutant mouse embryos (Fig 2i). High speed live video imaging of KVs of wild
270 type and *cph* homozygous mutants revealed that *cph* embryos exhibited a wide variation in
271 individual cilia motility patterns. Some cilia were motile, similar to wild type (Supplemental
272 Movie File 5), but others displayed abnormal motility, and immotile cilia were also observed
273 (Supplemental Movie File 6). Tracking movement of endogenous particles detectable in KV
274 fluid revealed a net anticlockwise movement in control KVs (Fig 4p, Supplemental Movie
275 File 7), but no such net movement was observed in *cph* mutant KVs (Fig 4q, Supplemental
276 Movie File 8), indicating a disruption in flow.
277
278 **Effect of the *Prpf8*^{N1531S} mutation on mRNA splicing**
279 Since PRPF8 is a component of the U5 snRNP that forms the spliceosomal catalytic centre, we
280 investigated whether the *Prpf8*^{N1531S} substitution affected splicing. Yeast cells containing a

281 *N1603S* missense substitution in yeast Prp8 (homologue of PRPF8), analogous to the mouse
282 *Prpf8*^{N1531S} allele, grew similarly to wild type yeast, indicating that the Prp8^{N1603S} mutation is
283 viable (Fig. 5a). We used the *ACT1-CUP1* splicing reporter (53) in Prp8^{N1603S} mutants to
284 determine which step of splicing was affected. Primer extension analysis of the *ACT1-CUP1*
285 splicing reporter revealed that with a branch site mutation (A259C), increased lariat
286 intermediate was detected in Prp8^{N1603S} cells compared to Prp8^{WT} (Fig. 5b), indicating the first
287 step of splicing had occurred. However, with a 3' splice site mutation (A302U), reduced levels
288 of mature mRNA were present in Prp8^{N1603S} cells (Fig. 5b), indicative of a defect in the second
289 step of splicing. This assay demonstrated that the Prp8^{N1603S} mutant is a first step allele of Prp8,
290 as it promoted the first step of splicing at the expense of the second step. We then examined
291 growth of Prp8^{N1603S} vs Prp8^{WT} yeast colonies with *ACT1-CUP1* reporters with either 3' splice
292 site, 5' splice site or branch point site mutations (Fig. 5c) on media with increasing
293 concentrations of copper. Copper tolerance is correlated with the amount of correctly spliced
294 mature *CUP1* transcript from the *ACT1-CUP1* construct and therefore the efficiency of splicing
295 (53). Prp8^{N1603S} cells could not tolerate copper as well as Prp8^{WT} cells, regardless of where the
296 mutation was in the *ACT1-CUP1* reporter construct. These data suggest that the Prpf8^{N1531S}
297 allele does not suppress any splice site mutations and is likely to be a hypomorphic mutation.
298

299 **RNA-seq analysis to identify splicing defects in *Prpf8*^{N1531S} mutant mouse embryos**

300 Mutations in PRPF8 are reported to cause mis-splicing in yeast, zebrafish and humans (7, 42,
301 52, 54). The yeast data we present suggest that the *Prpf8*^{N1531S} mutation could cause mis-
302 splicing in mouse embryos. We therefore performed bulk RNA-seq analysis on individual
303 whole embryos at E10.5: wild type (n=3), E10.5 *Prpf8*^{N1531S} mutants with correct heart looping
304 (n=3), and E10.5 *Prpf8*^{N1531S} mutants with reversed heart looping (n=3). Analysis of differential
305 exon skipping events between the two strains using the rMATS software package (55)

306 identified 498 statistically significant mid-penetrance exon skipping events (average difference
307 in exon inclusion between strains ≥ 20%; FDR-corrected p-value<0.05), across 431 unique
308 genes (Supplemental Table 2). Gene ontology (GO) enrichment analysis revealed the most
309 significant enrichment (24/51 genes, 2.43-fold) to be for genes associated with the biological
310 process "plasma membrane bounded cell projection morphogenesis", consistent with a model
311 of ciliary dysfunction (Supplemental Table 3).
312
313 To further narrow the field of key candidate genes that could underlie the laterality defects
314 detected in *Prpf8*^{N1531S} mutant mice, individual GO terms were attached to differentially spliced
315 genes identified by rMATS. Of the 431 unique genes harbouring exon skipping events, three -
316 *Arl13b*, *Rfx3* and *Rpgrip1l* - were upstream of or directly involved in "determination of
317 left/right symmetry", although only *Arl13b* was associated with "heart looping" and "left/right
318 axis specification". Because *Arl13b* is involved in both general L-R axis determination and
319 cardiac looping, and has known roles in the function of motile and non-motile cilia, the *Arl13b*
320 exon skipping event was prioritised for additional investigation.
321
322 In *Prpf8*^{N1531S} homozygous mutants, there is splicing between exons 8 and 10 of the *Arl13b*
323 gene in approximately 51% of reads mapping to the exon 8 splice donor site, whereas in wild
324 type embryos the corresponding event is detected in approximately 30% of reads (Fig. 6a).
325 This exon skipping event deletes the 69bp in-frame exon 9 from the transcript. An analysis of
326 the *Arl13b* transcript revealed that the omission of exon 9 is predicted to remove a 23 amino
327 acid segment of the Proline Rich Region from the C-terminal end of ARL13B (Fig. 6b). We
328 have termed this *Arl13b* transcript, lacking exon 9, the "short isoform", and the transcript
329 including exon 9 the "long isoform". The short isoform is not annotated in the fish or mouse
330 UCSC genome browsers, although a single mouse EST clone (DT914850) does have the same

331 sequence as the *Arl13b* short isoform we have identified. To our knowledge the function of this
332 isoform has not been studied previously. Using a single pair of PCR primers located in exons
333 8 and 10, we amplified both short and long *Arl13b* isoforms by RT-PCR in wildtype mouse
334 and zebrafish embryos (Fig. 6c). There was an increased ratio of the *Arl13b* short isoform
335 transcript to long transcript in both *Prpf8*^{N1531S} homozygous mouse and *cph* homozygous
336 mutant fish embryos (Fig. 6c). Sequencing of these RT-PCR products revealed the precise
337 deletion of exon 9 from the short isoform product (Fig. 6d). We also detected the *Arl13b* short
338 isoform in multiple adult mouse tissues, most notably in the testes (Fig. 6e-f).
339
340 **The ARL13B short isoform localises to cilia**
341 To determine if the shift in *ARL13B* isoform usage could affect phenotype, we generated
342 *ARL13B* short or long isoform human transcript sequences with N-terminal GFP fusions. These
343 were transfected into hTERT-RPE1 cells for comparison with endogenous ARL13B.
344 Endogenous ARL13B co-localised with acetylated tubulin at the cilium in hTERT-RPE1 cells
345 (Fig. 7a left). We detected protein produced from the GFP-tagged ARL13B short isoform co-
346 localised with endogenous acetylated tubulin at the cilium in hTERT-RPE1 cells (Fig. 7a
347 centre), demonstrating the short isoform produces a stable protein that is localised correctly.
348 Similar localisation results were seen for the GFP tagged ARL13B long isoform (Fig. 7a right).
349 The short isoform cilia localisation is consistent with the ARL13B cilia localisation signal
350 being within amino acids 347-363 (56), which are included in the short isoform transcript.
351
352 **Over-expression of the *arl13b* short isoform in zebrafish embryos mimics the *cph* mutant**
353 **phenotype**
354

355 We next sought to determine if increased expression of the zebrafish *arl13b* short isoform
356 causes cilia defects. We injected wild type zebrafish embryos with mRNA encoding a C-
357 terminal Arl13b-GFP fusion protein of either the short or long isoform. At 12 hours post-
358 injection, embryos exhibiting GFP were selected for further experiments. Half of the selected
359 embryos were fixed immediately for immunofluorescence to analyse Arl13b protein
360 localisation and KV cilia length, while the remaining embryos were monitored until 48 hours
361 post-injection to investigate phenotypes indicative of cilia dysfunction: cardiac looping and
362 pericardial oedema. In injected zebrafish embryos both Arl13b long and short isoform GFP
363 fusion proteins localised to KV cilia, showing co-localisation with acetylated tubulin (Fig 7b).
364 Measuring KV cilia length for each injection group, and plotting the average cilia length per
365 KV, revealed no significant change in KV cilia length in wild type fish injected with 80ng/ul
366 of *arl13b* long isoform GFP-tagged mRNA as compared to uninjected control fish (Fig 7c;
367 One-way ANOVA test, p=0.9901). However, cilia within the KV of fish injected with the
368 *arl13b* short isoform were significantly shorter than those in the uninjected control group (Fig
369 7c; One-way ANOVA test, p=0.0002), similar to findings for *cph* KV cilia length. The number
370 of cilia per KV was not significantly different between any of the groups (Fig 7d).
371
372 We next analysed cardiac looping at 48hpf in embryos injected with *arl13b* long and short
373 isoforms compared to uninjected controls. Immunofluorescence microscopy for the cardiac
374 marker MF20 revealed varied heart looping directionality. The uninjected control group heart
375 tube was correctly looped (Fig 7e top left); embryos from *arl13b* short isoform mRNA
376 injection showed a variety of cardiac laterality patterns including correct looping (34%),
377 delayed development and incomplete looping (66%) and reversed looping (2%) (Fig 7e; heart
378 looping direction listed on top left of image). No significant changes were seen in *arl13b* long
379 isoform injected embryos (Fig 7f; Fisher's exact test, p= 0.4949), whereas a significant

380 proportion of *arl13b* short isoform injected embryos displayed cardiac looping abnormalities
381 (Fig 7f; Fisher's exact test p<0.0001). Bright-field images of wild type uninjected fish
382 captured at 48hpf showed the expected cardiac morphology (Fig 7g top), whereas 56% of
383 *arl13b* short isoform injected embryos displayed pericardial oedema (Fig 7g bottom). The
384 percentage of the *arl13b* short isoform injected embryos showing pericardial oedema at 48hpf
385 was significantly increased compared to uninjected controls (Fig 7h; Fisher's exact test,
386 p<0.0001).
387
388 **Over-expression of *arl13b* long isoform rescued phenotypic defects of *prpf8* loss in**
389 **zebrafish embryos**
390 To determine if disruption of *arl13b* isoform usage is, at least in part, the mechanism
391 underlying the cardiac laterality defects in *cph* mutant fish, we utilised a *prpf8* splice
392 blocking morpholino (sbMO) targeting exon 7 (Supplemental Fig. 3), which provokes cardiac
393 laterality defects in injected zebrafish (57). KV cilia were identified by acetylated tubulin
394 immunofluorescence (Fig.8a). Compared to WT uninjected control embryos, the sbMO
395 injected embryo had significantly decreased KV cilia length (Fig. 8b; Unpaired t-test,
396 P<0.0001), but no significant difference was detected in cilia number per KV (Fig. 8c;
397 Unpaired t-test; p = 0.4868). Immunofluorescence microscopy at 48hpf showed cardiac
398 looping defects in embryos injected with *prpf8* sbMO (Fig. 8d), while co-injection of *prpf8*
399 sbMO with *arl13b* long isoform mRNA reduced the frequency of cardiac looping defects.
400 Co-injection of *prpf8* sbMO with *arl13b* short isoform mRNA did not rescue cardiac
401 development. Injection of a control MO showed no cardiac defects (Fig. 8d). Quantification
402 of cardiac defects revealed significant differences between the sbMO and control embryos
403 (Fig. 8e, Fisher's exact test p <0.0001), but not between embryos co-injected with *prpf8*
404 sbMO and *arl13b* long isoform mRNA when compared to control embryos (Fig. 8e; Fisher's

405 exact test, p >0.05). Additionally, a high incidence of severe pericardial oedema and tail
406 curvature defects was seen in embryos injected solely with *prpf8* sbMO, but embryos co-
407 injected with *prpf8* sbMO and *arl13b* long isoform mRNA exhibited a significant reduction
408 in the percentage of these defects (Fig. 8f-g; Fisher's exact test p <0.0001). The 72hpf
409 survival rate for *prpf8* sbMO embryos co-injected with *arl13b* long isoform mRNA was
410 significantly increased compared to *prpf8* sbMO injection alone (Fig. 8h; Fisher's exact test p
411 <0.0001). Morphological analysis of wild type uninjected control embryos or embryos co-
412 injected with *prpf8* sbMO and *arl13b* long isoform mRNA did not reveal obvious anatomical
413 defects (Fig. 8i) at 72hpf, whereas *prpf8* sbMO injected embryos exhibited pericardial
414 oedema (black arrowhead), head morphological defects (blue arrowhead), eye defects (green
415 arrowhead) and tail defects (orange arrowhead), as did embryos co-injected with *prpf8* sbMO
416 and *arl13b* short isoform mRNA.
417
418 **The ARL13B short isoform displays reduced binding to IFT-B1 complex proteins**
419 The short isoform of ARL13B lacks part of the proline rich region near the C-terminus of the
420 protein. The proline rich region binds IFT46 and IFT56 (58), components of the IFT-B1
421 complex involved in anterograde ciliary trafficking (59). We therefore sought to examine
422 differences in protein interactions between the long and short isoforms of ARL13B. Using a
423 GFP-trap system (60), we expressed either the GFP tag alone, or human long or short
424 ARL13B-GFP fusion protein isoforms in RPE1 cells, followed by GFP affinity purification-
425 mass spectrometry of three biological replicates. Network analysis of biological processes
426 that are enriched in proteins associated with the long isoform compared to the short isoform
427 revealed a network associated with cilia function (Fig. 8j; Supplemental Fig. 5). The short
428 isoform of ARL13B is depleted for binding to IFT22, IFT25, IFT46, IFT52, IFT56, IFT70a,
429 IFT74, and IFT81, which are all proteins found within the IFT-B1 complex (Fig. 8k;

430 Supplemental Fig. 5). Overall, these data suggest that the correct balance between ARL13B

431 isoforms is critical for maintaining cilia structure and function during development.

432

433 **Discussion**

434 We report a novel, evolutionarily conserved role for *Prpf8* in LRO cilia function and
435 determination of organ laterality in vertebrate embryos. We identified a shift in *Arl13b* isoform
436 usage as a potential mechanism explaining the laterality defects observed in *Prpf8* mutant
437 mouse and zebrafish embryos. Consistent with this finding, *Arl13b* mouse mutants (61, 62)
438 display cardiac looping defects, highly reminiscent of *Prpf8*^{N1531S} embryos described here (Fig
439 1), supporting the hypothesis that altered *Arl13b* isoform usage can perturb left-right axis
440 formation and embryonic development. We did not observe changes in PRPF8 protein
441 localisation to cilia (Supplemental Fig 2), suggesting that any as yet undefined ciliary, non-
442 splicing roles of PRPF8 (12) may be intact in the *Prpf8*^{N1531S} homozygous mouse mutant.

443

444 To our knowledge, other characterised mouse strains with mutations in *Prpf8* do not resemble
445 the *Prpf8*^{N153S} embryonic lethal laterality defect phenotype that we have detected (63-65).
446 Previously characterised mutants were generated to model human RP, containing variants in
447 the globular Jab1/MPN domain of PRPF8 (10). The N1531S mutation lies within the linker
448 domain of PRPF8, near the endonuclease-like domain (43), and thus may have a different effect
449 on PRPF8 function than mutations in the Jab1/MPN domain. Although many missense variants
450 throughout yeast Prp8 have been characterised (42), additional study is needed in mammalian
451 models to reveal the complexity of transcriptome and phenotypic defects that may arise from
452 variants in differing protein domains. However, an iPSC model of a heterozygous *PRPF8*
453 c.6926 A > C (p.H2309P) RP-associated mutation caused impaired alternative splicing and
454 enhanced cryptic splicing predominantly in ciliary and retinal-specific transcripts (11), which
455 is consistent with findings from the mouse N1531S variant.
456 Although we have shown several aspects of the *Prpf8*^{N1531S} and *cph* mutant phenotypes are
457 recapitulated by over-expression of the *arl13b* short isoform mRNA, we cannot exclude

458 contributions from other genes to the mutant phenotypes. For example, we detected splicing
459 alterations in the transcription factor *Rfx3* in *Prpf8*^{N1531S} mutants. *Rfx3* knockout embryos have
460 laterality and node cilia elongation defects (66), but their overall morphology, frequency of
461 situs inversus and incompletely penetrant embryonic lethality (66) are dissimilar to the
462 phenotypes of *Prpf8*^{N1531S} and *cph* mutants.
463
464
465 We demonstrated that increased usage of a previously uncharacterised transcript isoform of
466 *arl13b*, lacking exon 9, disrupted ciliogenesis and provoked laterality defects when over-
467 expressed in wild type zebrafish. We detect the short isoform in all tissues tested, in varying
468 ratios compared to the long isoform. Additional research is needed to reveal the roles of the
469 two different ARL13B isoforms in different tissues and cell types. In humans, pathological
470 variants in many ciliary genes, including *ARL13B*, cause Joubert syndrome (6, 67, 68), a well-
471 recognized ciliopathy (69). Laterality defects have been reported in some Joubert syndrome
472 patients, although individuals with laterality defects did not have variants in *ARL13B* (70).
473 Interactions between ARL13B and the IFT complex govern the speed of IFT entry into cilia,
474 and consequently, ciliary length (36, 71). Mutations in *Arl13b* and some IFT components in
475 zebrafish and mouse have been noted to result in short cilia (62, 72-74), suggesting that a
476 similar mechanism may play a role in the reduction in cilia length in zebrafish KV cilia in
477 embryos over-expressing the *arl13B* short isoform mRNA. Additionally, missense variants in
478 IFT52 cause cilia elongation defects in IMCD3 cells (75). Although the short isoform of the
479 ARL13B protein identified in *Prpf8*^{N1531S} and *cph* mutants localises to cilia, we demonstrated
480 that its interactions with IFT-B components, including IFT52, are reduced. Thus, the shorter
481 cilia detected in mutant LROs are consistent with a loss of IFT function.
482

483 Cilia motility is driven by dynein function. We found motility defects in the LRO cilia in
484 both *Prpf8*^{N1531S} mutant mouse and *cph* fish embryos, yet the mouse node cilia appear to have
485 intact dynein inner and outer arms. Defective cilia motility with preservation of dynein
486 protein cilia localisation has previously been reported for *Dnaaf1*^{m4Bei} and *Lrrc48*^{m6Bei} mouse
487 mutants (76). Therefore, although the mechanism for cilia motility defects in *Prpf8* mutants is
488 not fully understood, there is a precedent for the disruption of cilia motility without dynein
489 arrangement defects. Additionally, the shift in ARL13B isoform usage results in reduced
490 binding between ARL13B and IFT-B complex proteins, including IFT74, IFT22 and IFT81.
491 IFT74 has physical interactions with IFT22 and IFT81, and a binary interaction with the inner
492 dynein arm protein DNALI1 (77) proposed to be required for cilia motility (78). Patients with
493 hypomorphic IFT74 variants show cilia motility defects, although not laterality defects (79).
494 A mouse IFT74 mouse null mutant shows mid-gestation lethality and cardiac oedema, but
495 laterality defects were not reported for these mutants (80). To our knowledge, it is not clear if
496 these proteins are localised to the LRO cilia during development, but this is an area for future
497 investigation. There is high conservation of protein content between cilia of different types
498 and different localisations (81), which notably includes ARL13B and the IFT proteins found
499 to be affected in PRPF8 mutants. Together, our findings suggest a mechanistic link between
500 altered PRPF8 protein function in the spliceosome, aberrant splicing of *Arl13b* transcript and
501 abnormalities in IFT and cilia function, culminating in conserved laterality defects in mutant
502 embryos.
503

504 **Materials and Methods**

505

506 ***l11Jus27* mouse model**

507 The *Prpf8*^{N1531S} strain is derived from the *l11Jus27* strain (32) and was backcrossed for at
508 least 2 generations to the 129S5/SvEvBrd line carrying the chromosomal inversion
509 Inv(11)8Brd$^{Trp\text{-}Wnt3}$, and then maintained through sibling intercrosses for at least 6
510 generations. Mouse colonies were maintained at the Biological Service Facility at the
511 University of Manchester, UK, according to Home Office requirements and with local ethical
512 approval (project licence number PP3720525). Mice were euthanised using a Schedule 1
513 method following UK Home Office regulations. Genotyping was performed as described
514 (41).

515

516 **Mouse embryo morphological analysis**

517 Embryos were isolated from timed pregnant female mice by dissection in PBS. Morphology
518 was analysed using a Leica dissecting microscope. Whole embryos were incubated in 1
519 ng/mL propidium iodide staining solution for 5 min, followed by 3 X 5 minute washes in
520 PBS, before imaging with a DAPI filter to identify heart tube laterality.

521

522 **Genome sequencing**

523 Genomic DNA was extracted from an E10.5 *l11Jus27* homozygous embryo using ISOLATE
524 II Genomic DNA Kit (Bioline). 1 µg of DNA was sequenced at The Manchester Centre for
525 Genomic Medicine (MCGM), Saint Mary's Hospital, Manchester, UK, on the Illumina HiSeq
526 platform. Reads were then aligned to the mouse MGSCv37 (mm9) genome assembly. Variants
527 in the candidate region on chr 11 were analysed. Known variants in 129 and B6 mouse strains

528 were excluded, as well as variants present in fewer than 50% of reads. The remaining variants
529 were annotated with Ensembl Variant Effect Predictor (VEP). A single novel exonic mutation
530 was present in 100% of mapped reads: an A to G transition at position Chr11: 75,391,978
531 (mm39). Sanger sequencing was performed to verify the sequence change in three additional
532 individual embryos (University of Manchester Genomic Technologies Core Facility).

533

534 **Mutation Analysis**

535 Conservation of protein sequence across different species was evaluated using multiple
536 sequence alignments in Clustal Omega (https://www.ebi.ac.uk/Tools/msa/clustalo/). Mutation
537 pathogenicity was predicted using SIFT (45) and PolyPhen2 (44). The Prpf8 protein
538 Alphafold structure was downloaded from AlphFold Protein Structure Database:
539 https://alphafold.ebi.ac.uk/entry/Q6P2Q9; and opened as entry AF-Q99PV0-F1-v4 in
540 PyMOL software (Version 3.1.1).

541

542 **Quantitative PCR**

543 *Prpf8* expression was quantified using a *Prpf8* TaqMan probe (Applied Biosystems Cat:
544 4331182) on a DNA Engine Opticon 2 continuous fluorescence detector (BioRad). The raw
545 data were processed on Opticon monitor 3 (BioRad) software and subsequently analysed
546 using Excel (Microsoft). Samples were normalised against expression levels of *Gapdh*
547 (primers listed in Supplemental Table 4).

548

549 **Scanning Electron Microscopy**

550 Embryos at were dissected in PBS and fixed in 2.5% glutaraldehyde, 4% paraformaldehyde in
551 0.1M HEPES (pH7.4) at 4°C from overnight up to 1 month. Embryos were then washed 5x 5
552 minutes in dH_2O, then incubated for 1 hour in OsO_4 in 0.1M HEPES (pH7.4). They were then

553 washed 5x 5 minutes in dH_2O and taken through an ethanol dehydration series before critical
554 point drying. Embryos were mounted ventral side up on stubs using graphite sticky tape and
555 conductive epoxy. Samples were imaged at high vacuum at 10KV on a Quanta FEG 250
556 electron microscope (FEI).
557
558 **Transmission Electron Microscopy**
559 Embryos were fixed and processed as for SEM. Embedding, sectioning and imaging was
560 performed as previously described (82). Samples were imaged on a Tecnai 12 Biotwin
561 transmission electron microscope.
562
563 **Nodal cilia videomicroscopy**
564 E8.25 embryos were dissected individually in warmed DMEM modified with HEPES without
565 glutamine and sodium pyruvate (Sigma D6171), supplemented with 10% heat inactivated FBS
566 (Gibco 10500064). Embryos at the 1-3 somite stage were selected for imaging and were
567 transferred to a homemade chamber slide with the ventral node facing the microscope
568 objective. To visualise the nodal flow, the media was replaced with a 1:100 dilution of latex
569 microbeads (Sigma L1398) in media. A coverslip was then placed over the chamber and the
570 slides were incubated at 37°C for 10 minutes before imaging on a Leica DMRB at 40X using
571 a Leica MC170HD camera. Five-minute videos were taken using VGA2USB (Epiphan Video)
572 with an MPEG4 decompressor at maximum quality. Video analysis was performed using the
573 Manual Tracker plugin from Fiji (83). Movies were converted to .tiff stacks of 150 frames from
574 the first minute of filming and the paths of 5 beads were tracked.
575
576 For visualising nodal cilia movement directly, embryos were imaged on a Nikon TE2000 PFS
577 microscope using a 100x/1.49 Apo TIRF objective. Videos lasting 20 seconds were collected

578 on a FASTCAM SA3 (Photron) at 125 frames per seconds and analysed using Fiji. Imaging
579 data were enhanced for visual analysis by performing 11-frame running-average background
580 subtraction followed by inversion and thresholding, using custom routines coded in MATLAB
581 R2015a with Image Processing toolbox (Mathworks, Natick, MA). Motile cilia were counted
582 manually by inspection of 125 frame (1 s) sequences taken at each focal plane.
583

584 **Mouse and zebrafish embryo whole mount *in situ* hybridisation**

585 Whole mount *in situ* hybridisation was performed according to established protocols in mouse
586 (84) and zebrafish (85). Control and mutant embryos were pooled and hybridised with
587 digoxigenin labelled probes and incubated with alkaline phosphatase conjugated anti-
588 digoxigenin antibodies. Hybridised embryos were then developed with NBT-BCIP until
589 desired staining was achieved. *In situ* probes were synthesised using either plasmid or PCR
590 templates. *In situ* probe primer sequences for PCR templates are listed in Supplemental Table
591 4.
592

593 **Mouse embryo immunofluorescence staining**

594 Antibodies used for immunostaining are found in Supplemental Table 5. Embryos previously
595 stored at -20C in methanol were rehydrated through a methanol series, washed 3x 20 minutes
596 in PBS and blocked for 90 minutes at room temperature in 5% horse serum and 0.5% Triton
597 X-100 in PBS. Control and mutant embryos were pooled and then incubated overnight at 4°C
598 in 5% horse serum, 0.5% Triton X-100 in PBS with primary antibodies. Embryos were then
599 washed in 3x20 minutes in PBS and then incubated with secondary antibodies in PBS with 1%
600 horse serum for 2 hours at room temperature. Embryos were washed 3x10 minutes in PBS and
601 then incubated with Cy5 labelled streptavidin in PBS for 30 minutes. Embryos were washed
602 3x20 minutes in PBS with 1% horse serum and then stained with DAPI in PBS, before a final

603 10 minute wash in ice-cold PBS. Embryos were then individually placed in dishes of PBS and
604 the anterior portion of the embryo was removed. The posterior portion, including the node,
605 was transferred to a homemade chamber slide, excess PBS removed, and embryos mounted in
606 Prolong Gold Antifade (Life Sciences, P36934). The anterior portion was used to re-genotype
607 the samples. The embryo was arranged ventral side up and a coverslip was placed on top, with
608 gentle pressure applied to remove bubbles and excess mounting medium. Slides were cured
609 for at least 2 days at room temperature.
610
611 Embryos were imaged on a Leica TCS SP5 AOBS upright confocal microscope using a
612 63x/1.40 HCX PL Apo objective and a 2.0x digital zoom using sequential imaging in a
613 2048x2048 format.
614
615 **Mouse Embryo Western Blot**
616 E10.5 mouse embryos were lysed in RIPA buffer supplemented with protease inhibitors. As
617 described earlier, protein lysates were separated by SDS-PAGE and transferred to PVDF
618 membranes (86). Western blotting was performed using antibodies against PRPF8 and GAPDH
619 (loading control). Signal detection was carried out using LI-COR Odyssey system and the
620 image was quantified using the LI-COR Image Studio software.
621
622 **PRPF8 FLAG-tagged plasmid generation and transfection**
623 IMAGE clone 5587081 containing human PRPF8 was used for generating PRPF8 constructs.
624 Mouse and human PRPF8 proteins differ by only 3 of the total 2335 amino acids. We
625 generated the N1531S variant by site directed mutagenesis (Q5 Site Directed Mutagenesis
626 kit; NEB), and corrected a A759G missense sequence change present in the IMAGE clone.
627 Primer sequences are listed in Supplemental Table 4. To correct the A759G sequence

628 change, primers creating a new restriction site for Eco47III were utilised. Rather than
629 creating the exact *l11Jus27* mutation (aat to agt), we used an alternate codon sequence which
630 generated the same amino acid mutation (aat to agc), but created a BseYI restriction site
631 allowing screening for colonies containing the correct mutation prior to sequence verification.
632 Oligonucleotides containing a FLAG tag sequence, a start codon, a Kozak sequence and a
633 Cla1 restriction site were cloned into the corrected wild type and the N1531S mutant PRPF8
634 plasmids at an AgeI restriction site.
635
636 **PRPF8 protein stability analysis**
637 HEK293T cells were cultured as described previously (86). The cells were seeded at a
638 density of $0.1x10^6$/well in 6 well plates for transfection. The next day the cells were
639 transfected with 2µg of *PRPF8* WT-Flag or N1531S-Flag plasmid using Fugene HD reagent
640 (Promega). 48hours later the transfection media was removed, and cells were treated with
641 100µM cycloheximide in cell culture media. The cells were lysed at different time points (0,
642 4, 8, 16 hours) in RIPA buffer. The immunoblotting was performed using anti Flag and anti
643 β-Actin (ACTB) antibodies as described previously (86). Signal detection was carried out
644 using LI-COR Odyssey system. Image was quantified using the LI-COR Image Studio
645 software.
646
647 **Zebrafish *cph* mutants**
648 Fish were maintained at the Institute of Molecular and Cell Biology, A*STAR Zebrafish
649 Facility and the University of Manchester Biological Services Facility (IMCB protocol
650 number: 221702 and Manchester project licence PP8367714) at a temperature of 28.5°C and a
651 standard light/dark cycle of 14 hours and 10 hours respectively. Pair mating was used to obtain

652 embryos. Embryos were incubated at 28.5°C in egg water containing methylene blue until the
653 desired stage.
654
655 **Genotyping *cph* mutants**
656 *cph* mutant zebrafish were genotyped by PCR amplification of exon 8 and 9 of the *prpf8* gene
657 (52), followed by purification using QIAquick PCR and Gel Purification Kit (Cat. No 28104),
658 and a restriction digest using AccI enzyme performed as per manufacturer's instructions.
659 Samples were ran on a 2% agarose gel. WT fish produced one band, heterozygotes produced 3
660 bands and *cph* homozygotes produced 2 bands (Supplemental Figure 6).
661
662 **Zebrafish whole mount immunofluorescence**
663 Embryos were transferred into a glass cavity dish and rehydrated from methanol by washing
664 in consecutively lower methanol concentrations (75%, 50%, 25%) in PBS. Embryos were
665 subsequently washed in PBS for 3x 5 minutes. PBS was removed and embryos treated with -
666 20°C acetone and placed at -20°C for 7 minutes (this step was not used for embryos fixed with
667 Dent's fix). Embryos were washed for 3x 5 minutes in room temperature PBS. Embryos were
668 incubated for 1 hour at room temperature in blocking buffer (2% sheep serum in PBDT) on an
669 orbital shaker at 70 rpm. Blocking buffer was removed and primary antibody diluted in PBDT
670 added (Supplemental Table 5). Embryos were placed on an orbital shaker at 70rpm overnight
671 at 4°C. The following morning primary antibody was removed and embryos washed in room
672 temperature PBDT 3x 30 minutes on an orbital shaker at 70rpm. PBDT was removed and
673 secondary antibodies diluted in fresh PBDT were added. Embryos were placed on an orbital
674 shaker at 70rpm for 5 hours at room temperature. During the last 30 minutes DAPI was added
675 (1:2000). Secondary antibodies were removed and embryos washed 3x 30 minutes with room

676 temperature PBDT. PBDT was removed and embryos were submerged in 70% glycerol for
677 storage at 4°C. Primary antibodies for immunostaining found in Supplemental Table 5.
678
679 **Measurement of Node and KV LRO Cilia**
680 To detect nodal cilia, mouse 1-4 somite embryos were stained for Ac-tubulin and DAPI and
681 subsequently mounted and imaged as described earlier. Zebrafish 14hpf embryos were stained
682 with Ac-tubulin, Gamma-Tubulin and DAPI as per zebrafish whole mount
683 immunofluorescence protocol. KV was dissected out and mounted on a slide. Mounted KVs
684 were imaged on an Olympus Fluoview 1000 confocal microscope and Leica TCS SP8 AOBS
685 inverted confocal microscope at x100 zoom and a z-stack images were taken for the entire
686 vesicle. Mouse and fish images were processed using ImageJ with Simple Neurite Tracer
687 utilised to measure each cilium from the base to the tip in 3 dimensions. After imaging, embryos
688 were retrieved from the slides, washed with PBS and used for genotyping.
689
690 **Zebrafish KV Motile Cilia Live Imaging**
691 Embryos from *cph* heterozygous fish incross were collected and placed in egg water at 28.5°C
692 to develop until ~14hpf. A mould designed to hold embryos was made using 2% agarose in
693 egg water and left to set. Once embryos had developed to the correct stage, embryos with well-
694 developed KVs were dechorionated and placed into the mould. Embryos were covered with
695 egg water and placed on a Zeiss Imager M2 live imaging microscope. All embryos were imaged
696 on a 100x water dipping lens at ~150-200fps using Metamorph software. Embryos were then
697 placed into separate wells of a 24 well plate coated with 2% agarose in egg water to stop the
698 embryos sticking to the plastic. Recordings of each embryo were saved by well number.
699 Embryos were left to develop until the mutant phenotype became apparent and recordings were
700 correlated with the phenotype. Recordings were analysed using ImageJ and slowed to 15fps.

701

702 **RNA sequencing analysis**

703 Total RNA was isolated from wild type and *Prpf8*^{N1531S} mutant embryos at E10.5 using Trizol
704 according to manufacturer's instructions (Ambion). RNA was prepared from 3 embryos of
705 each genotype. RNA quality was evaluated using TapeStation.

706

707 Paired-end RNA sequencing of E10.5 mouse embryo samples was performed on the Illumina
708 HiSeq 3000 platform in the University of Leeds Next Generation Sequencing Facility. The
709 FASTQ files were deposited into the Sequence Read Archive (SRA) under the accession
710 number PRJNA690736. For RNA-Seq data, the adapter sequences were removed using
711 Cutadapt (1.9.1) (87) , and the filtering and trimming of sequences were done using
712 PRINSEQ (0.20.4) (88). The clean reads were aligned to the UCSC mouse genome (mm10)
713 (89) using STAR (2.5.1b) (90). The processing of BAM files was done using SAMtools
714 (1.3.1) (91) and only uniquely mapped alignments were kept for further analysis. Read counts
715 for protein-coding genes were generated through the featureCounts function provided by
716 Rsubread package (1.22.0) (92) and RPKM values were calculated using rpkm function of
717 edgeR package (3.14.0) (93). For those genes with RPKM >= 1 in at least one sample, a
718 value of 1 was added to all RPKM values before the log2 transformation. Principal
719 component analysis was carried out on the quantile normalised values and the first two
720 principal components were plotted. We observed three expression outliers based on poor
721 clustering: one from the wild type, one from the mutant correct looped, and one from the
722 mutant reversed loop strain, which were excluded from downstream splicing analysis.
723 Differential expression between groups of samples were conducted using DESeq2 package
724 (1.12.0) (94) based on the raw counts for genes. Differential alternative splicing events were
725 identified using rMATS (4.0.2) (55).

726

727

728 **Differential splicing analysis**

729 Splicing events in RNA-seq data from the three wild-type day 10.5 embryos were compared
730 against those in the three *Prpf8*^{N1531S} mutant embryos using rMATS v4.0.2. Results were
731 filtered to retain only splicing events exhibiting a difference in exon level inclusion
732 (IncLevelDifference ≥ 0.2 or ≤ -0.2), and an FDR < 0.05.

733

734 **Gene ontology (GO) analysis**

735 GO enrichment was performed using the PANTHER GO overrepresentation test
736 (http://geneontology.org/). Genes harbouring exon skipping events with a difference in
737 inclusion of ≥ 20% between the wild-type and *Prpf8*^{N1531S} mutant embryos were evaluated
738 against all *Mus musculus* genes in the GO Ontology Database. GO terms exhibiting a positive
739 enrichment were retained. Genes present in the rMATS output were annotated with their
740 respective GO annotations, retaining those annotations labelled as "biological_process" and
741 with relationships to their genes of "involved_in" and "enables".

742

743 ***Arl13b* isoform RT-PCR quantification**

744 qPCR could not be utilised for isoform quantification as no primers or probe could be generated
745 specifically for the "short" isoform of *Arl13b*. To quantify relative isoform levels, *Arl13b* RT-
746 PCR was performed with a species-specific single primer set (Supplemental Table 4) that
747 amplifies both the short and long isoforms. Gel electrophoresis was carried out to separate
748 isoforms, with gels imaged on a Li-Cor Odessey and optical intensity quantified using Image
749 Studio software with background gel intensity set to 0. The ratio of optical intensity of the
750 "short" isoform to the "long" isoform was then calculated for each sample, and fold change

751 calculated for the mutants as compared to wild type. Data are shown for at least three individual
752 embryos of each genotype.
753
754 **Generation of Prp8^{N1603S} yeast and yeast splicing analysis**
755 The N1603S mutation was introduced into pRS413-PRP8 by site directed mutagenesis (95).
756 The pRS413-PRP8, pRS413-PRP8^{N1603S} or pRS413 plasmid was transformed into a haploid
757 yeast strain where both the *CUP1* and *PRP8* genes were deleted and *PRP8* function was
758 complemented with pRS416-PRP8. Growth on 5-fluoro-orotic acid (5-FOA) containing plates
759 was used to select against and remove the complementing pRS416-PRP8 plasmid to leave the
760 pRS413 plasmids as the sole source of *PRP8* and growth properties observed at 16°C, 30°C
761 and 37°C. The resulting haploid strains with pRS413-PRP8 or pRS413-PRP8^{N1603S} were
762 transformed with different *ACT1-CUP1* splicing reporters (53) and growth assayed on plates
763 with increasing concentrations of $CuSo_4$. Primer extension was carried out (53) to monitor the
764 two steps of splicing from the *ACT1-CUP1* splicing reporters.
765
766 **ARL13B mammalian expression constructs**
767 The long and short isoforms of human *ARL13B* were synthesised by GenScript and inserted as
768 a N-terminal EGFP fusion protein into a mammalian expression plasmid with a CMV
769 promoter. Sequence was confirmed by whole plasmid sequencing (Genewiz).
770
771 **hTERT-RPE1 cell transfections and imaging**
772 **Cell Culture**
773 hTERT-RPE1 cells were cultured in DMEM/F12 media containing 10% (v/v) foetal bovine
774 serum (FBS) and 2mM L-glutamine. Cells were split 1 in 10 using trypsin-EDTA when
775 reaching 80-90% confluence. Cells were incubated at 37℃, 5% CO2.

776 **Transfection**

777 hTERT-RPE1 cells were transfected with *GFP*-tagged *ARL13B* long and short isoform plasmid
778 using Lipofectamine™ 3000 Transfection Reagent (Invitrogen), following the manufacturer's
779 instructions. The transfection medium was replaced with 0.2% FBS starvation medium after
780 24h and cells were incubated a further 24h-48h to induce cilia before use.

781 **Immunofluorescence**

782 hTERT-RPE1 cells on coverslips were fixed in 4% paraformaldehyde for 10 minutes at RT.
783 Cells were then permeabilised with 0.3% Triton X-100 in PBS for 30 minutes at RT and
784 blocked in SuperBlock blocking buffer (Thermo Fisher Scientific) for 1h at RT. Cells were
785 incubated in the primary antibody (mouse anti-acetylated tubulin, Supplemental Table 5)
786 diluted in 'Solution 1 for primary antibody' from SignalBoost Immunoreaction Enhancer Kit
787 (Merck) overnight at 4°C before washing three times in 0.1% PBS-Tween20 and incubation in
788 the secondary antibody (Alexa Fluor donkey anti-mouse 594 IgG (H+L) AffiniPure, Jackson
789 ImmunoResearch) diluted in 'Solution 2 for secondary antibody' from SignalBoost
790 Immunoreaction Enhancer Kit for 1h at RT. Cells were then washed three times in 0.1% PBS-
791 Tween20 followed by incubation in DAPI for 5min. Coverslips were air dried before mounting
792 with Prolong Gold antifade reagent (Thermo Fisher Scientific). Cells were imaged on a Leica
793 TCS SP8 AOBS inverted confocal microscope. Images were processed with Fiji.

794

795 **Zebrafish *arl13b* mRNA injections**

796 Zebrafish *arl13b* long isoform was amplified by RT-PCR from zebrafish cDNA and cloned
797 into PCS2+ xlt Vector using Hifi DNA assembly kit (New England Biolabs). Inverse PCR was
798 used to generate the *arl13b* short isoform lacking exon 9. Plasmid inserts were sequenced
799 (Genewiz). RNA was transcribed from a linearised plasmid using the mMessage Machine kit
800 (Invitrogen). RNA was precipitated and stored at -80°C. RNA was diluted in DEPC-H_2O to the

801 desired concentration, and 0.5nl of 80ng/µl *arl13b* long or short isoform mRNAs was
802 microinjected into zebrafish embryos at the single cell stage. Injected embryos were collected
803 and placed in fresh egg water and left to develop at 28.5°C to the desired developmental stages.
804 Embryos with green florescence were selected at 12hpf (using a LEICA M165 FC
805 stereomicroscope) for use in further analysis.
806
807 ***prpf8* splice blocking morpholino knockdown and rescue**
808 Splicing blocking morpholinos targeting exon 7 of zebrafish *prpf8* (57) were synthesized by
809 GeneTools (Supplemental Table 4). A 300nmol *prpf8* sbMO stock solution was made in sterile
810 water to a final concentration of 1mM, and zebrafish embryos were injected with 0.5 nl of a
811 1:2 dilution of sbMO stock at the single-cell stage. For the rescue of *prpf8* morphants, after the
812 injection of morpholinos, 0.5nl of *arl13b-GFP* long isoform or *arl13b-GFP* short isoform
813 mRNA (200ng/ul) was injected into each morpholino injected embryo. Wild type embryos
814 were injected with 0.5nl of a 1:2 dilution of Gene Tools standard MO as a control
815 (Supplemental Table 4). Embryos were cultured in fish embryo medium (0.3g/L NaCl) until
816 12hpf. Embryos exhibiting green fluorescence by microscopy (LEICA M165 FC) were
817 selected for further study. Embryos were incubated at 28.5°C until the desired developmental
818 stages to observe the phenotype using brightfield microscopy (LEICA M80).
819
820 **ARL13B Affinity purification-mass spectrometry**
821 **Cloning and Vector Preparation**
822 For GFP-trap affinity purification-mass spectrometry (AP-MS) analysis, the *ARL13B*_long
823 and *ARL13B*_short isoforms were cloned into the CMV-EGFP-RGCC-SV40 poly(A)-
824 NeoR/KanR vector (gifted by Prof. Ben Goult, University of Liverpool) by replacing the
825 RGCC gene sequence with the respective *ARL13B* isoform sequences. Cloning was

826 performed using SacI-HF and XmaI restriction enzymes (New England Biolabs, NEB, USA)
827 and HiFi DNA Assembly, according to the manufacturer's instructions. The control vector,
828 expressing GFP alone, was generated by excising the RGCC sequence using MfeI-HF and
829 BspEI restriction enzymes (NEB) and inserting a short filler sequence using HiFi DNA
830 Assembly.

831 **Transfection**

832 $1x10^6$ hTERT-RPE1 cells were seeded in 10cm plates one day before transfection.
833 Transfection was performed using Lipofectamine 3000 transfection reagent (Invitrogen,
834 L3000015) according to the manufacturer's protocol. For each plate, 8µg of plasmid DNA
835 was used. After 10 hours of transfection, the transfection medium was replaced with fresh
836 complete medium to allow the cells to recover. At 24 hours post-transfection, the medium
837 was changed to low-serum medium (0.2% FBS) for 24 hours to induce ciliogenesis before
838 harvesting.

839 **Cell Harvesting and Peptide Sample Preparation**

840 hTERT-RPE1 cells expressing GFP-vector, GFP-ARL13B short isoform and GFP-ARL13B
841 long isoform were harvested in RIPA buffer (Thermo Scientific, 89900, USA) supplemented
842 with EDTA-free protease inhibitor cocktail (Roche, REF: 04693159001), PhosSTOP
843 phosphatase inhibitor (Roche, REF: 04906837001), DNase (50 U/ml, Thermo Scientific, Cat:
844 EN0521), and 2.5 mM MgCl2 (NEB, B0510A). Cell lysates were clarified by centrifugation.
845 GFP pull-down, trypsin digestion, and peptide preparation for AP-MS analysis were
846 performed according to the protocol provided with the ChromoTek iST Myc-Trap® Kit
847 (Proteintech, Cat no: ytak-iST).

848 **Mass Spectrometry Analysis**

849 Samples were analyzed using a Thermo Exploris 480 mass spectrometer equipped with a
850 FAIMS Pro interface and coupled to a U3000 nanoUPLC system. Each sample underwent a

851 1-hour LC-MS run, performed at the Biological Mass Spectrometry Facility, University of
852 Manchester.

853 **Data Analysis**

854 Mass spectrometry data were processed using Fragpipe (v22.0), incorporating MSFragger
855 (v4.1), IonQuant (v1.10.27), and DiaTracer (v1.1.5) within a label-free quantification (LFQ)
856 and match-between-runs (MBR) workflow. MaxLFQ intensity values were exported from
857 Fragpipe and analyzed using the R Shiny application "Manchester Proteome Profiler"
858 (developed by Dr. Stuart Cain, unpublished). Proteins were identified as significantly
859 enriched based on a fold-change threshold of >4 and an adjusted p-value cutoff of <0.05.

860

861 **Statistical analysis**

862 Statistical analyses and the generation of graphs was performed on GraphPad Prism 10 for
863 Mac, GraphPad Software, La Jolla, California, USA.

864

865 **Data Availability**

866

867 RNAseq data can be accessed in the Sequence Reads Archive. Mass spectrometry data is
868 available in the PRIDE database. Supplemental Movie Files are located on Zenodo with doi:
869 10.5281/zenodo.15482494.

870

871 **Acknowledgements**

872 We thank Monica Justice for the *l11Jus27* mouse line and Graham Lieschke for the *cph* fish
873 line. We thank Dominic Norris for advice on EM imaging of cilia, and for the *Nodal*, *Cerl2*,
874 *Lefty1* and *Lefty2* mouse *in situ* hybridisation probe plasmids. We thank Megan Davey for
875 advice on immunostaining of cilia. We thank Adam Hurlstone, Martin Lowe, Shane Herbert

and Karel Dorey for advice on zebrafish experiments and access to equipment. Some computational data analysis work was undertaken on ARC4, part of the High-Performance Computing facility at the University of Leeds, UK. The authors wish to thank the staff in the University of Manchester FBMH Electron Microscopy Core Facility, Biological Mass Spectrometry Facility (RRID: SCR_020987), and Peter March in the BioImaging Core Facility for their assistance, and the Wellcome Trust for funding to support core facility equipment. We thank Stuart Cain for assistance with mass spectrometry data analysis and Xiaofan Xiong for uploading data to PRIDE. We thank the Biological Services Facility at the University of Manchester for mouse and fish husbandry. We thank the IMCB zebrafish facility for maintenance of zebrafish strains.

Funding Statement

This work was supported by BHF grants PG/06/144/21898, PG/10/87/28624 and PG/18/28/33632 to KEH, Fight for Sight grant 5163/5164 to KEH, and funding from the Agency for Science, Technology and Research (A*STAR) of Singapore to S.R. KEH and BK acknowledge support from a British Heart Foundation Research Excellence Award (RE/24/130017). BK was supported by a BHF personal chair (CH/13/2/30154). DWM was supported by a University of Manchester-A*STAR Research Attachment Program (ARAP) Ph.D. fellowship. This work was supported in part by the Wellcome Trust [105610/Z/14/Z]. MB, LS and KM were supported by BBSRC DTP studentships awarded to the University of Manchester. MTG and DJS acknowledge EPSRC award EP/N021096/1.

Author Contributions

FJ, MB, DM, WMSQ, CFR, GT, JZ, JL, KM, LAS, NA, DVL, EJRV, DW, MTG, BB, KS, AV, DS, KEH performed research. FJ, MB, DM, KEH wrote original manuscript draft. BK, MJH, JE, DS, CAJ, ROK, SR and KEH provided supervision and obtained funding. All authors read and edited the manuscript draft and approved submission.

Competing Interests

No competing interests

Materials and Correspondence - KEH

References

1. Mirvis M, Stearns T, James Nelson W. Cilium structure, assembly, and disassembly regulated by the cytoskeleton. The Biochemical journal. 2018;475(14):2329-53.
2. Shinohara K, Hamada H. Cilia in Left-Right Symmetry Breaking. Cold Spring Harb Perspect Biol. 2017;9(10).
3. Waters AM, Beales PL. Ciliopathies: an expanding disease spectrum. Pediatr Nephrol. 2011;26(7):1039-56.
4. Ferrari S, Di Iorio E, Barbaro V, Ponzin D, Sorrentino FS, Parmeggiani F. Retinitis pigmentosa: genes and disease mechanisms. Curr Genomics. 2011;12(4):238-49.
5. Wheway G, Lord J, Baralle D. Splicing in the pathogenesis, diagnosis and treatment of ciliopathies. Biochim Biophys Acta Gene Regul Mech. 2019;1862(11-12):194433.
6. Maxwell DW, O'Keefe RT, Roy S, Hentges KE. The role of splicing factors in retinitis pigmentosa: links to cilia. Biochem Soc Trans. 2021;49(3):1221-31.
7. Tanackovic G, Ransijn A, Thibault P, Abou Elela S, Klinck R, Berson EL, et al. PRPF mutations are associated with generalized defects in spliceosome formation and pre-mRNA splicing in patients with retinitis pigmentosa. Hum Mol Genet. 2011;20(11):2116-30.
8. Korir PK, Roberts L, Ramesar R, Seoighe C. A mutation in a splicing factor that causes retinitis pigmentosa has a transcriptome-wide effect on mRNA splicing. BMC Res Notes. 2014;7:401.
9. Arzalluz-Luque A, Cabrera JL, Skottman H, Benguria A, Bolinches-Amoros A, Cuenca N, et al. Mutant PRPF8 Causes Widespread Splicing Changes in Spliceosome Components in Retinitis Pigmentosa Patient iPSC-Derived RPE Cells. Front Neurosci. 2021;15:636969.
10. Malinova A, Cvackova Z, Mateju D, Horejsi Z, Abeza C, Vandermoere F, et al. Assembly of the U5 snRNP component PRPF8 is controlled by the HSP90/R2TP chaperones. J Cell Biol. 2017;216(6):1579-96.
11. Atkinson R, Georgiou M, Yang C, Szymanska K, Lahat A, Vasconcelos EJR, et al. PRPF8-mediated dysregulation of hBrr2 helicase disrupts human spliceosome kinetics and 5 -splice-site selection causing tissue-specific defects. Nat Commun. 2024;15(1):3138.
12. Wheway G, Schmidts M, Mans DA, Szymanska K, Nguyen TM, Racher H, et al. An siRNA-based functional genomics screen for the identification of regulators of ciliogenesis and ciliopathy genes. Nat Cell Biol. 2015;17(8):1074-87.
13. Kim JH, Ki SM, Joung JG, Scott E, Heynen-Genel S, Aza-Blanc P, et al. Genome-wide screen identifies novel machineries required for both ciliogenesis and cell cycle arrest upon serum starvation. Biochim Biophys Acta. 2016;1863(6 Pt A):1307-18.
14. Xu K, Ou G. Cilia regeneration requires an RNA splicing factor from the ciliary base. Cell Regen. 2022;11(1):29.
15. Okada Y, Takeda S, Tanaka Y, Belmonte JI, Hirokawa N. Mechanism of nodal flow: a conserved symmetry breaking event in left-right axis determination. Cell. 2005;121(4):633-44.
16. Sulik K, Dehart DB, Iangaki T, Carson JL, Vrablic T, Gesteland K, Schoenwolf GC. Morphogenesis of the murine node and notochordal plate. Dev Dyn. 1994;201(3):260-78.
17. Nonaka S, Tanaka Y, Okada Y, Takeda S, Harada A, Kanai Y, et al. Randomization of left-right asymmetry due to loss of nodal cilia generating leftward flow of extraembryonic fluid in mice lacking KIF3B motor protein. Cell. 1998;95(6):829-37.
18. Okada Y, Nonaka S, Tanaka Y, Saijoh Y, Hamada H, Hirokawa N. Abnormal nodal flow precedes situs inversus in iv and inv mice. Mol Cell. 1999;4(4):459-68.
19. McGrath J, Somlo S, Makova S, Tian X, Brueckner M. Two populations of node monocilia initiate left-right asymmetry in the mouse. Cell. 2003;114(1):61-73.

960 20. Katoh TA, Omori T, Mizuno K, Sai X, Minegishi K, Ikawa Y, et al. Immotile cilia
961 mechanically sense the direction of fluid flow for left-right determination. Science.
962 2023;379(6627):66-71.
963 21. Marques S, Borges AC, Silva AC, Freitas S, Cordenonsi M, Belo JA. The activity of
964 the Nodal antagonist Cerl-2 in the mouse node is required for correct L/R body axis. Genes
965 Dev. 2004;18(19):2342-7.
966 22. Collignon J, Varlet I, Robertson EJ. Relationship between asymmetric nodal
967 expression and the direction of embryonic turning. Nature. 1996;381(6578):155-8.
968 23. Nakamura T, Saito D, Kawasumi A, Shinohara K, Asai Y, Takaoka K, et al. Fluid
969 flow and interlinked feedback loops establish left-right asymmetric decay of Cerl2 mRNA.
970 Nat Commun. 2012;3:1322.
971 24. Saijoh Y, Adachi H, Sakuma R, Yeo CY, Yashiro K, Watanabe M, et al. Left-right
972 asymmetric expression of lefty2 and nodal is induced by a signaling pathway that includes
973 the transcription factor FAST2. Mol Cell. 2000;5(1):35-47.
974 25. Norris DP, Brennan J, Bikoff EK, Robertson EJ. The Foxh1-dependent autoregulatory
975 enhancer controls the level of Nodal signals in the mouse embryo. Development.
976 2002;129(14):3455-68.
977 26. Yamamoto M, Mine N, Mochida K, Sakai Y, Saijoh Y, Meno C, Hamada H. Nodal
978 signaling induces the midline barrier by activating Nodal expression in the lateral plate.
979 Development. 2003;130(9):1795-804.
980 27. Shiratori H, Sakuma R, Watanabe M, Hashiguchi H, Mochida K, Sakai Y, et al. Two-
981 step regulation of left-right asymmetric expression of Pitx2: initiation by nodal signaling and
982 maintenance by Nkx2. Mol Cell. 2001;7(1):137-49.
983 28. Kitamura K, Miura H, Miyagawa-Tomita S, Yanazawa M, Katoh-Fukui Y, Suzuki R,
984 et al. Mouse Pitx2 deficiency leads to anomalies of the ventral body wall, heart, extra- and
985 periocular mesoderm and right pulmonary isomerism. Development. 1999;126(24):5749-58.
986 29. Semina EV, Reiter R, Leysens NJ, Alward WL, Small KW, Datson NA, et al. Cloning
987 and characterization of a novel bicoid-related homeobox transcription factor gene, RIEG,
988 involved in Rieger syndrome. Nat Genet. 1996;14(4):392-9.
989 30. Liu C, Liu W, Lu MF, Brown NA, Martin JF. Regulation of left-right asymmetry by
990 thresholds of Pitx2c activity. Development. 2001;128(11):2039-48.
991 31. Franco D, Sedmera D, Lozano-Velasco E. Multiple Roles of Pitx2 in Cardiac
992 Development and Disease. J Cardiovasc Dev Dis. 2017;4(4).
993 32. Kile BT, Hentges KE, Clark AT, Nakamura H, Salinger AP, Liu B, et al. Functional
994 genetic analysis of mouse chromosome 11. Nature. 2003;425(6953):81-6.
995 33. Hentges KE, Nakamura H, Furuta Y, Yu Y, Thompson DM, O'Brien W, et al. Novel
996 lethal mouse mutants produced in balancer chromosome screens. Gene Expr Patterns.
997 2006;6(6):653-65.
998 34. Cevik S, Hori Y, Kaplan OI, Kida K, Toivenon T, Foley-Fisher C, et al. Joubert
999 syndrome Arl13b functions at ciliary membranes and stabilizes protein transport in
1000 Caenorhabditis elegans. J Cell Biol. 2010;188(6):953-69.
1001 35. Song P, Perkins BD. Developmental expression of the zebrafish Arf-like small
1002 GTPase paralogs arl13a and arl13b. Gene Expr Patterns. 2018;29:82-7.
1003 36. Lu H, Toh MT, Narasimhan V, Thamilselvam SK, Choksi SP, Roy S. A function for
1004 the Joubert syndrome protein Arl13b in ciliary membrane extension and ciliary length
1005 regulation. Dev Biol. 2015;397(2):225-36.
1006 37. Gigante ED, Taylor MR, Ivanova AA, Kahn RA, Caspary T. ARL13B regulates
1007 Sonic hedgehog signaling from outside primary cilia. Elife. 2020;9.
1008 38. Pintado P, Sampaio P, Tavares B, Montenegro-Johnson TD, Smith DJ, Lopes SS.
1009 Dynamics of cilia length in left-right development. R Soc Open Sci. 2017;4(3):161102.

1010 39. Cevik S, Sanders AA, Van Wijk E, Boldt K, Clarke L, van Reeuwijk J, et al. Active
1011 transport and diffusion barriers restrict Joubert Syndrome-associated ARL13B/ARL-13 to an
1012 Inv-like ciliary membrane subdomain. PLoS Genet. 2013;9(12):e1003977.
1013 40. Fu W, Wang L, Kim S, Li J, Dynlacht BD. Role for the IFT-A Complex in Selective
1014 Transport to the Primary Cilium. Cell Rep. 2016;17(6):1505-17.
1015 41. Ridge LA, Mitchell K, Al-Anbaki A, Shaikh Qureshi WM, Stephen LA, Tenin G, et
1016 al. Non-muscle myosin IIB (Myh10) is required for epicardial function and coronary vessel
1017 formation during mammalian development. PLoS Genet. 2017;13(10):e1007068.
1018 42. Grainger RJ, Beggs JD. Prp8 protein: at the heart of the spliceosome. RNA.
1019 2005;11(5):533-57.
1020 43. Galej WP, Oubridge C, Newman AJ, Nagai K. Crystal structure of Prp8 reveals active
1021 site cavity of the spliceosome. Nature. 2013;493(7434):638-43.
1022 44. Adzhubei I, Jordan DM, Sunyaev SR. Predicting functional effect of human missense
1023 mutations using PolyPhen-2. Curr Protoc Hum Genet. 2013;Chapter 7:Unit7 20.
1024 45. Ng PC, Henikoff S. SIFT: Predicting amino acid changes that affect protein function.
1025 Nucleic Acids Res. 2003;31(13):3812-4.
1026 46. Kennedy MP, Omran H, Leigh MW, Dell S, Morgan L, Molina PL, et al. Congenital
1027 heart disease and other heterotaxic defects in a large cohort of patients with primary ciliary
1028 dyskinesia. Circulation. 2007;115(22):2814-21.
1029 47. Rachel RA, Li T, Swaroop A. Photoreceptor sensory cilia and ciliopathies: focus on
1030 CEP290, RPGR and their interacting proteins. Cilia. 2012;1(1):22.
1031 48. Valcarcel J, Malumbres M. Splicing together sister chromatids. EMBO J.
1032 2014;33(22):2601-3.
1033 49. Tsiairis CD, McMahon AP. An Hh-dependent pathway in lateral plate mesoderm
1034 enables the generation of left/right asymmetry.
1035 50. Nowotschin S, Liao J, Gage PJ, Epstein JA, Campione M, Morrow BE. Tbx1 affects
1036 asymmetric cardiac morphogenesis by regulating Pitx2 in the secondary heart field.
1037 51. Tissier-Seta JP, Mucchielli ML, Mark M, Mattei MG, Goridis C, Brunet JF. Barx1, a
1038 new mouse homeodomain transcription factor expressed in cranio-facial ectomesenchyme
1039 and the stomach. Mech Dev. 1995;51(1):3-15.
1040 52. Keightley MC, Crowhurst MO, Layton JE, Beilharz T, Markmiller S, Varma S, et al.
1041 In vivo mutation of pre-mRNA processing factor 8 (Prpf8) affects transcript splicing, cell
1042 survival and myeloid differentiation. FEBS Lett. 2013;587(14):2150-7.
1043 53. Lesser CF, Guthrie C. Mutational analysis of pre-mRNA splicing in Saccharomyces
1044 cerevisiae using a sensitive new reporter gene, CUP1. Genetics. 1993;133(4):851-63.
1045 54. Kurtovic-Kozaric A, Przychodzen B, Singh J, Konarska MM, Clemente MJ, Otrock
1046 ZK, et al. PRPF8 defects cause missplicing in myeloid malignancies. Leukemia.
1047 2015;29(1):126-36.
1048 55. Shen S, Park JW, Lu ZX, Lin L, Henry MD, Wu YN, et al. rMATS: robust and
1049 flexible detection of differential alternative splicing from replicate RNA-Seq data. Proc Natl
1050 Acad Sci U S A. 2014;111(51):E5593-601.
1051 56. Mahajan D, Madugula V, Lu L. Rab8 and TNPO1 are ciliary transport adaptors for
1052 GTPase Arl13b by interacting with its RVEP motif containing ciliary targeting sequence. J
1053 Biol Chem. 2023;299(5):104604.
1054 57. Boylan M. A Novel Point Mutation in Prpf8 Causes Defects in Left-Right Axis
1055 Establishment in the Mouse. United Kingdom: University of Manchester; 2015.
1056 58. Nozaki S, Katoh Y, Terada M, Michisaka S, Funabashi T, Takahashi S, et al.
1057 Regulation of ciliary retrograde protein trafficking by the Joubert syndrome proteins
1058 ARL13B and INPP5E. J Cell Sci. 2017;130(3):563-76.

1059 59. Lacey SE, Foster HE, Pigino G. The molecular structure of IFT-A and IFT-B in
1060 anterograde intraflagellar transport trains. Nat Struct Mol Biol. 2023;30(5):584-93.
1061 60. Zhang S, Williamson NA, Bogoyevitch MA. Complementary proteomics strategies
1062 capture an ataxin-1 interactome in Neuro-2a cells. Sci Data. 2018;5:180262.
1063 61. Garcia-Garcia MJ, Eggenschwiler JT, Caspary T, Alcorn HL, Wyler MR, Huangfu D,
1064 et al. Analysis of mouse embryonic patterning and morphogenesis by forward genetics. Proc
1065 Natl Acad Sci U S A. 2005;102(17):5913-9.
1066 62. Caspary T, Larkins CE, Anderson KV. The graded response to Sonic Hedgehog
1067 depends on cilia architecture. Dev Cell. 2007;12(5):767-78.
1068 63. Graziotto JJ, Farkas MH, Bujakowska K, Deramaudt BM, Zhang Q, Nandrot EF, et
1069 al. Three gene-targeted mouse models of RNA splicing factor RP show late-onset RPE and
1070 retinal degeneration. Invest Ophthalmol Vis Sci. 2011;52(1):190-8.
1071 64. Krausova M, Kreplova M, Banik P, Cvackova Z, Kubovciak J, Modrak M, et al.
1072 Retinitis pigmentosa-associated mutations in mouse Prpf8 cause misexpression of circRNAs
1073 and degeneration of cerebellar granule cells. Life Sci Alliance. 2023;6(6).
1074 65. Farkas MH, Lew DS, Sousa ME, Bujakowska K, Chatagnon J, Bhattacharya SS, et al.
1075 Mutations in pre-mRNA processing factors 3, 8, and 31 cause dysfunction of the retinal
1076 pigment epithelium.
1077 66. Bonnafe E, Touka M, AitLounis A, Baas D, Barras E, Ucla C, et al. The transcription
1078 factor RFX3 directs nodal cilium development and left-right asymmetry specification.
1079 67. Cantagrel V, Silhavy JL, Bielas SL, Swistun D, Marsh SE, Bertrand JY, et al.
1080 Mutations in the cilia gene ARL13B lead to the classical form of Joubert syndrome. Am J
1081 Hum Genet. 2008;83(2):170-9.
1082 68. Thomas S, Cantagrel V, Mariani L, Serre V, Lee JE, Elkhartoufi N, et al.
1083 Identification of a novel ARL13B variant in a Joubert syndrome-affected patient with retinal
1084 impairment and obesity. Eur J Hum Genet. 2015;23(5):621-7.
1085 69. Spahiu L, Behluli E, Grajcevci-Uka V, Liehr T, Temaj G. Joubert syndrome:
1086 Molecular basis and treatment. J Mother Child. 2022;26(1):118-23.
1087 70. Gana S, Serpieri V, Valente EM. Genotype-phenotype correlates in Joubert
1088 syndrome: A review. Am J Med Genet C Semin Med Genet. 2022;190(1):72-88.
1089 71. Engel BD, Ludington WB, Marshall WF. Intraflagellar transport particle size scales
1090 inversely with flagellar length: revisiting the balance-point length control model. J Cell Biol.
1091 2009;187(1):81-9.
1092 72. Pazour GJ, Dickert BL, Vucica Y, Seeley ES, Rosenbaum JL, Witman GB, Cole DG.
1093 Chlamydomonas IFT88 and its mouse homologue, polycystic kidney disease gene tg737, are
1094 required for assembly of cilia and flagella. J Cell Biol. 2000;151(3):709-18.
1095 73. Krock BL, Perkins BD. The intraflagellar transport protein IFT57 is required for cilia
1096 maintenance and regulates IFT-particle-kinesin-II dissociation in vertebrate photoreceptors. J
1097 Cell Sci. 2008;121(11):1907-15.
1098 74. Hou Y, Qin H, Follit JA, Pazour GJ, Rosenbaum JL, Witman GB. Functional analysis
1099 of an individual IFT protein: IFT46 is required for transport of outer dynein arms into
1100 flagella. J Cell Biol. 2007;176(5):653-65.
1101 75. Dupont MA, Humbert C, Huber C, Siour Q, Guerrera IC, Jung V, et al. Human IFT52
1102 mutations uncover a novel role for the protein in microtubule dynamics and centrosome
1103 cohesion. Hum Mol Genet. 2019;28(16):2720-37.
1104 76. Ha S, Lindsay AM, Timms AE, Beier DR. Mutations in Dnaaf1 and Lrrc48 Cause
1105 Hydrocephalus, Laterality Defects, and Sinusitis in Mice. G3 (Bethesda). 2016;6(8):2479-87.
1106 77. McCafferty CL, Papoulas O, Lee C, Bui KH, Taylor DW, Marcotte EM, Wallingford
1107 JB. An amino acid-resolution interactome for motile cilia identifies the structure and function
1108 of ciliopathy protein complexes. Dev Cell. 2025;60(6):965-78 e3.

78. Rashid S, Breckle R, Hupe M, Geisler S, Doerwald N, Neesen J. The murine Dnali1 gene encodes a flagellar protein that interacts with the cytoplasmic dynein heavy chain 1. Mol Reprod Dev. 2006;73(6):784-94.
79. Fassad MR, Rumman N, Junger K, Patel MP, Thompson J, Goggin P, et al. Defective airway intraflagellar transport underlies a combined motile and primary ciliopathy syndrome caused by IFT74 mutations. Hum Mol Genet. 2023;32(21):3090-104.
80. Bakey Z, Cabrera OA, Hoefele J, Antony D, Wu K, Stuck MW, et al. IFT74 variants cause skeletal ciliopathy and motile cilia defects in mice and humans. PLoS Genet. 2023;19(6):e1010796.
81. Wheway G, Parry DA, Johnson CA. The role of primary cilia in the development and disease of the retina. Organogenesis. 2014;10(1):69-85.
82. Canty EG, Lu Y, Meadows RS, Shaw MK, Holmes DF, Kadler KE. Coalignment of plasma membrane channels and protrusions (fibripositors) specifies the parallelism of tendon. J Cell Biol. 2004;165(4):553-63.
83. Schindelin J, Arganda-Carreras I, Frise E, Kaynig V, Longair M, Pietzsch T, et al. Fiji: an open-source platform for biological-image analysis. Nat Methods. 2012;9(7):676-82.
84. Henrique D, Adam J, Myat A, Chitnis A, Lewis J, Ish-Horowicz D. Expression of a Delta homologue in prospective neurons in the chick. Nature. 1995;375(6534):787-90.
85. Thisse B, Pflumio, S., Fürthauer, M., Loppin, B., Heyer, V., Degrave, A., Woehl, R., Lux, A., Steffan, T., Charbonnier, X.Q. and Thisse, C. Expression of the zebrafish genome during embryogenesis (NIH R01 RR15402). [ZFIN Direct Data Submission]. In press 2001.
86. Wood KA, Rowlands CF, Qureshi WMS, Thomas HB, Buczek WA, Briggs TA, et al. Disease modeling of core pre-mRNA splicing factor haploinsufficiency. Hum Mol Genet. 2019;28(22):3704-23.
87. Martin M. Cutadapt removes adapter sequences from high-throughput sequencing reads. 2011. 2011;17(1):3.
88. Schmieder R, Edwards R. Quality control and preprocessing of metagenomic datasets. Bioinformatics. 2011;27(6):863-4.
89. Frankish A, Diekhans M, Ferreira AM, Johnson R, Jungreis I, Loveland J, et al. GENCODE reference annotation for the human and mouse genomes. Nucleic Acids Res. 2019;47(D1):D766-D73.
90. Dobin A, Davis CA, Schlesinger F, Drenkow J, Zaleski C, Jha S, et al. STAR: ultrafast universal RNA-seq aligner. Bioinformatics. 2013;29(1):15-21.
91. Li H, Handsaker B, Wysoker A, Fennell T, Ruan J, Homer N, et al. The Sequence Alignment/Map format and SAMtools. Bioinformatics. 2009;25(16):2078-9.
92. Liao Y, Smyth GK, Shi W. The R package Rsubread is easier, faster, cheaper and better for alignment and quantification of RNA sequencing reads. Nucleic Acids Res. 2019;47(8):e47.
93. Robinson MD, McCarthy DJ, Smyth GK. edgeR: a Bioconductor package for differential expression analysis of digital gene expression data. Bioinformatics. 2010;26(1):139-40.
94. Love MI, Huber W, Anders S. Moderated estimation of fold change and dispersion for RNA-seq data with DESeq2. Genome Biol. 2014;15(12):550.
95. Kunkel TA, Roberts JD, Zakour RA. Rapid and efficient site-specific mutagenesis without phenotypic selection. Methods Enzymol. 1987;154:367-82.

1156 **Figures and Legends**

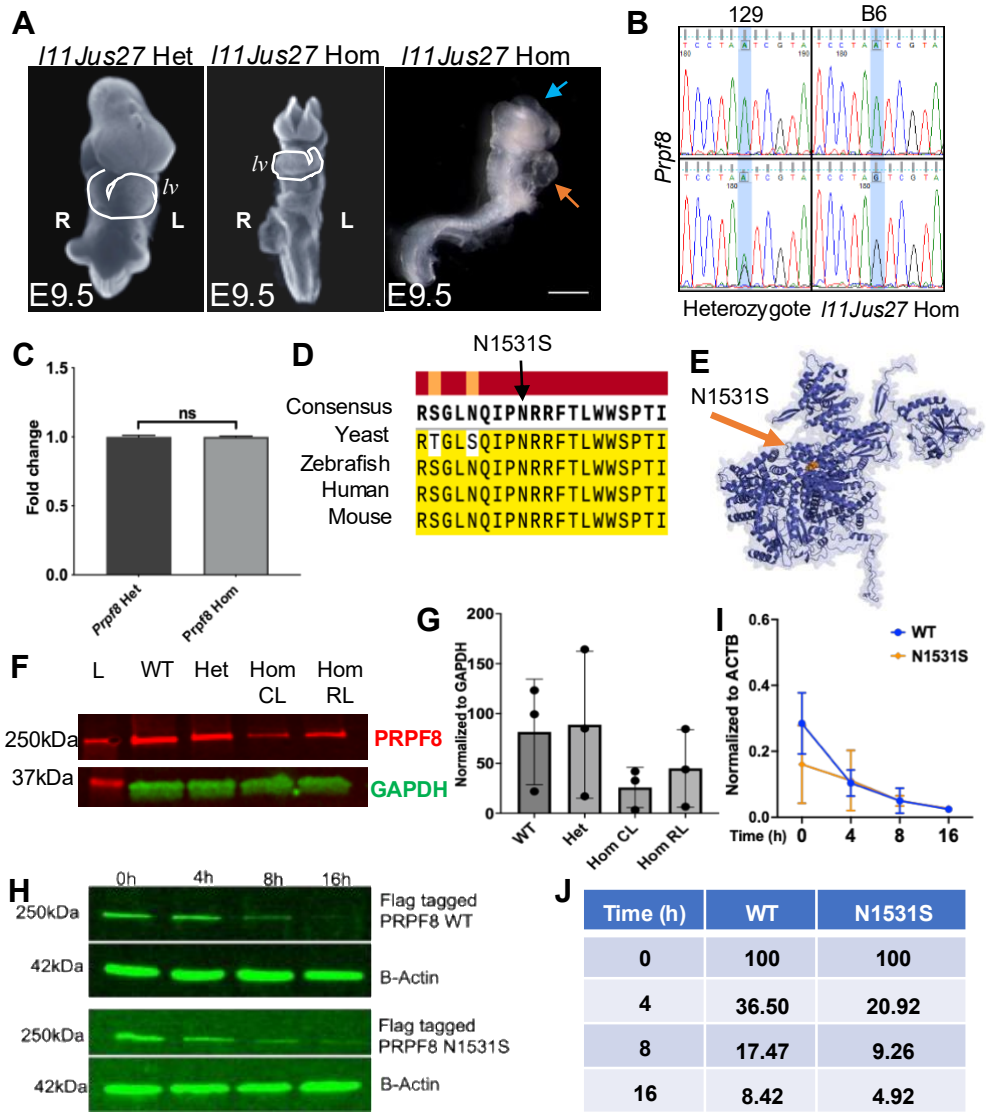

Time (h)	WT	N1531S
0	100	100
4	36.50	20.92
8	17.47	9.26
16	8.42	4.92

1157

1158 **Fig 1. Genetic analysis of *l11Jus27* mice.** A) Propidium iodide stained E9.5 *l11Jus27*
1159 heterozygote showing correct leftward looping of heart (heart tube outlined in white; lv= left
1160 ventricle), *l11Jus27* homozygote showing reversed looping of heart (heart tube outlined in
1161 white; lv = morphological left ventricle), *l11Jus27* homozygote showing open neural tube (blue
1162 arrow) and distended heart tube (orange arrow). B) Sanger sequencing of individual mouse
1163 embryos confirming that the N1531S substitution is present in heterozygous embryos and
1164 homozygous embryos carrying the *l11Jus27* phenotype, but not in wild type mice from either
1165 a 129S5 (129) or C57BL/6 (B6) background. C) qPCR quantification of *Prpf8* expression

levels in *Prpf8*^{N1531S} heterozygous and homozygous mutant whole embryos at E10.5. Results from the average of three biological and three technical replicates are presented. Expression levels were normalised to *Gapdh* expression. D) Clustal analysis of PRPF8 protein orthologues in mouse, zebrafish, human and *Saccharomyces cerevisiae* showing that residue 1531 is conserved across multiple eukaryotes. Identical residues are highlighted in yellow. E) Protein structure of PRPF8 with amino acid replacement at residue 1531 shown in red. F) Western blot confirms PRPF8 protein is present in *Prpf8*^{N1531S} heterozygotes and homozygous mutant whole embryos with either correct heart looping (CL) or reversed heart looping (RL) at E10.5. G) Quantification of PRPF8 protein levels from Western blots. Each sample was normalised to GAPDH protein expression levels. H) Western blot analysis of mammalian cells transfected with epitope tagged PRPF8 constructs at specified time points after cycloheximide treatment. I) Quantification of PRPF8 expression levels normalised to ACTB for wild type and PRPF8^{N1531S} alleles following cycloheximide treatment. J) PRPF8 WT and N1531S protein half-life percentage decrease as compared to protein levels present at 0h. Numbers report percentage of original protein remaining at each time point. Differences in degradation rate are non-significant (Wilcoxon test p=0.125).

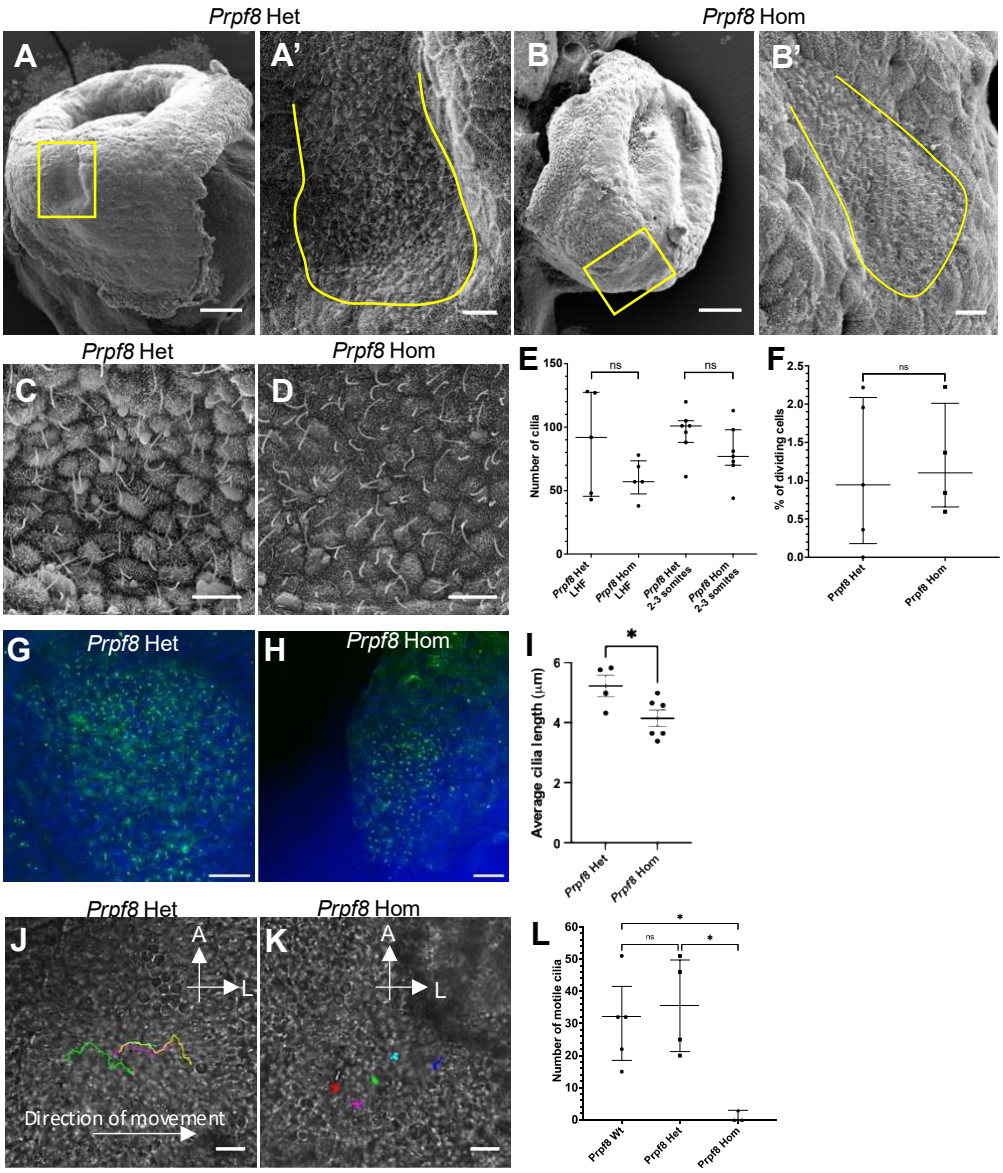

1184

1185 **Fig 2. Analysis of *Prpf8*^{N1531S} heterozygous and homozygous node cilia.** A-D) SEM images

1186 of 2-3 somite stage *Prpf8*^{N1531S} heterozygous (A, C) and homozygous (B, D) mouse embryos.

1187 A) The pit shape of the node (yellow boxes) is obvious in *Prpf8*^{N1531S} heterozygotes.

1188 *Prpf8*^{N1531S} mutant embryos (B) have a flat node. Scale bar = 100µm. A', B') Higher

1189 magnification images of boxed region in A and B. The node (yellow outline) is ciliated in both

1190 genotypes. Scale bar = 10um. C-D) Higher magnification images of the node at 2-3 somite

1191 stage. No gross morphological difference in cilia was observed between genotypes. Scale bar

1192 = 5µm. E) Heterozygotes and homozygotes have equivalent numbers of nodal cilia at the LHF

1193 and 2-3 somite stage (unpaired t-test). F) Cell proliferation was unaltered between genotypes

1194 (unpaired t-test). G-H) Mouse node cilia labelled with acetylated tubulin in heterozygous
1195 control (G) and *Prpf8*^{N1531S} mutant embryos (H). Nuclei are stained with DAPI. I) Measurement
1196 of node cilia length reveals that *Prpf8*^{N1531S} mutant cilia are significantly shorter than
1197 heterozygous controls (unpaired t-test p=0.0408). J-K) Tracking the travel over time of five
1198 microbeads in the node revealed directional movement in *Prpf8*^{N1531S} heterozygotes (J) but only
1199 Brownian motion in *Prpf8*^{N1531S} homozygotes (K). Direction of movement is indicated with an
1200 arrow. A= anterior, L = left. L) Quantification of motile nodal cilia in *Prpf8*$^{+/+}$, *Prpf8*^{N1531S}
1201 heterozygous and *Prpf8*^{N1531S} homozygous embryos at the 2-3 somite stage revealed significant
1202 differences between the three genotypes (p=0.0058, Welch's ANOVA). Post-hoc testing with
1203 Dunnett's T3 test showed that the number of motile cilia in *Prpf8*^{N1531S} homozygotes was
1204 significantly lower compared to *Prpf8*$^{+/+}$ (p=0.0222) and *Prpf8*$^{N1531S/+}$ embryos (p=0.0487),
1205 but not between *Prpf8*$^{N1531S/+}$ and *Prpf8*$^{+/+}$ embryos (p=0.9332).
1206
1207
1208
1209

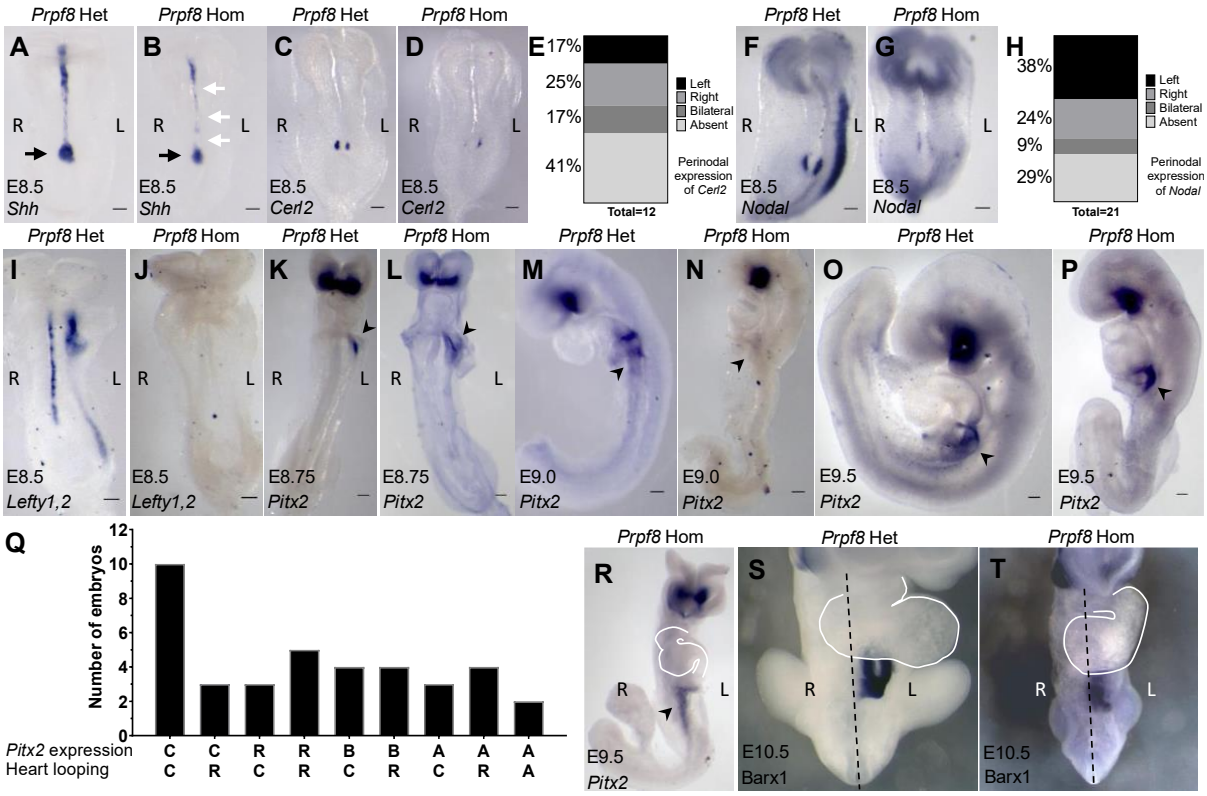

Fig 3. Wholemount *in situ* hybridisation expression analysis of laterality genes in *Prpf8*^{N1531S} heterozygous and homozygous mutant embryos. A) *Prpf8*^{N1531S} heterozygote showing *Shh* midline and node expression (black arrow). B) *Prpf8*^{N1531S} homozygote showing intact *Shh* expression at the node (black arrow), but discontinuous midline staining (white arrows). C) E8.5 *Prpf8*^{N1531S} heterozygote with upregulation of *Cerl2* on the right vs the left of the node. D) *Prpf8*^{N1531S} homozygote with reversed *Cerl2* expression. E) Graphical representation of *Cerl2* expression patterns seen in *Prpf8*^{N1531S} homozygotes revealing a high degree of variability. F) E8.5 *Prpf8*^{N1531S} heterozygote showing *Nodal* expression pattern with upregulation left of the node and left LPM. G) *Prpf8*^{N1531S} homozygote showing reduced and reversed perinodal *Nodal* expression and no expression in the LPM. H) Graphical representation of *Nodal* perinodal expression in *Prpf8*^{N1531S} homozygotes revealing variable expression patterns. I) E8.5 *Prpf8*^{N1531S} heterozygote showing *Lefty1, 2* expression along the midline and left LPM, detected with a probe complimentary to both mRNAs; no expression was detected in *Prpf8*^{N1531S} homozygotes (J). K-P) *Pitx2* expression in the LPM (black

1225 arrowheads) at E8.75 (K,L), E9.0 (M,N) and E9.5 (O,P) with *Prpf8*^{N1531S} heterozygotes
1226 showing left-sided *Pitx2* expression (K,M,O) and *Prpf8*^{N1531S} homozygotes showing
1227 randomised Pitx2 expression (L,N,P). Q) Graphical representation of data comparing sidedness
1228 of LPM *Pitx2* expression with heart looping direction at E9.5 revealing a disconnect between
1229 expression sidedness (*Pitx2*) and heart looping (heart). C= correct, R= reversed, B= bilateral,
1230 A= absent. R) E9.5 expression of *Pitx2* in *Prpf8*^{N1531S} homozygote showing discordance
1231 between heart looping and *Pitx2* expression sidedness (arrow). S,T) E10.5 expression of *Barx1*
1232 labelling the developing stomach in *Prpf8*^{N1531S} heterozygote (S) and in *Prpf8*^{N1531S}
1233 homozygote (T). Dashed line indicates the midline, and the heart is outlined in white. L= left,
1234 R= right. Scale bars = 0.5mm.
1235

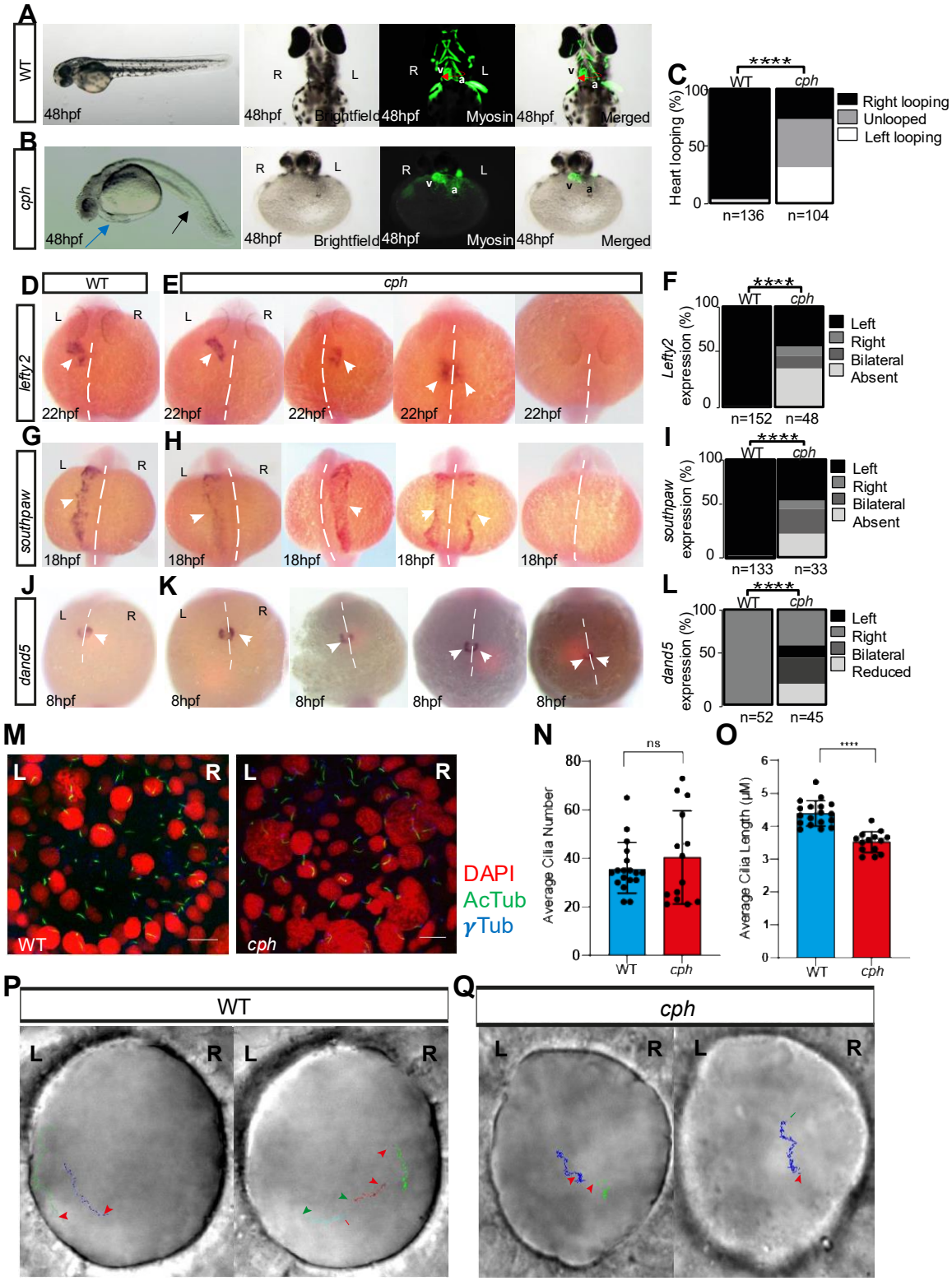

Fig 4. Developmental laterality and cilia defects in *cph* zebrafish. A) Wild type zebrafish at 48hpf with straight body axis (left panel). MF20 staining to identify heart tube is shown in green (right two panels). Red arrow shows looping direction of heart. B) *cph* mutant zebrafish

1240 with curled down body axis (black arrow) and pericardial oedema (blue arrow) indicative of
1241 cilia defects. MF20 staining shows delayed heart tube looping (green; right two panels). C) *cph*
1242 mutant fish show a significance increase in heart looping defects compared to wild type
1243 controls. D) Expression of the laterality gene *lefty2* in wild type zebrafish at 22hpf (white
1244 arrowheads indicate location of gene expression in panels E-L). E) Gene expression patterns
1245 of the laterality gene *lefty2* are altered in *cph* mutant fish, showing a variety of expression
1246 patterns. F) Statistical summary of *lefty2* expression pattern defects in *cph* fish. G) Expression
1247 of the laterality gene *southpaw* in wild type zebrafish at 18hpf. H) Gene expression patterns of
1248 the laterality gene *southpaw* are altered in *cph* mutant fish, showing a variety of expression
1249 patterns. I) Statistical summary of *southpaw* expression pattern defects in *cph* fish. J)
1250 Expression of the laterality gene *dand5* in wild type zebrafish at 8hpf. K) Gene expression
1251 patterns of the laterality gene *dand5* are altered in *cph* mutant fish, showing a variety of
1252 expression patterns. L) Statistical summary of *dand5* expression pattern defects in *cph* fish. M)
1253 Acetylated tubulin (green) and gamma tubulin (blue) staining in wild type fish KV (left) and
1254 *cph* fish KV (right). DAPI staining for nuclei is shown in red (Scale bar = 10μ). N)
1255 Quantification of average cilia number per KV between wild type control and *cph* fish. O)
1256 Quantification of average cilia length within individual KVs demonstrates *cph* KV cilia are
1257 significantly shorter than wild type KV cilia (n=14 and n=18 KVs respectively). Data are
1258 represented as mean ± SD. Significance was evaluated using unpaired t-test. $P<0.0001$ P) Still
1259 images from videos showing particle movement in wild type fish KV (representative of n=5,
1260 Scale bar = 10μm, Time lapsed = ~3s). Q) Still images from movies showing particle
1261 movement in *cph* fish KV (representative of n=5, Scale bar = 10μm, Time lapsed = ~3s). Green
1262 and red arrows indicate the start and end position of the bead, respectively. L left, R right.
1263

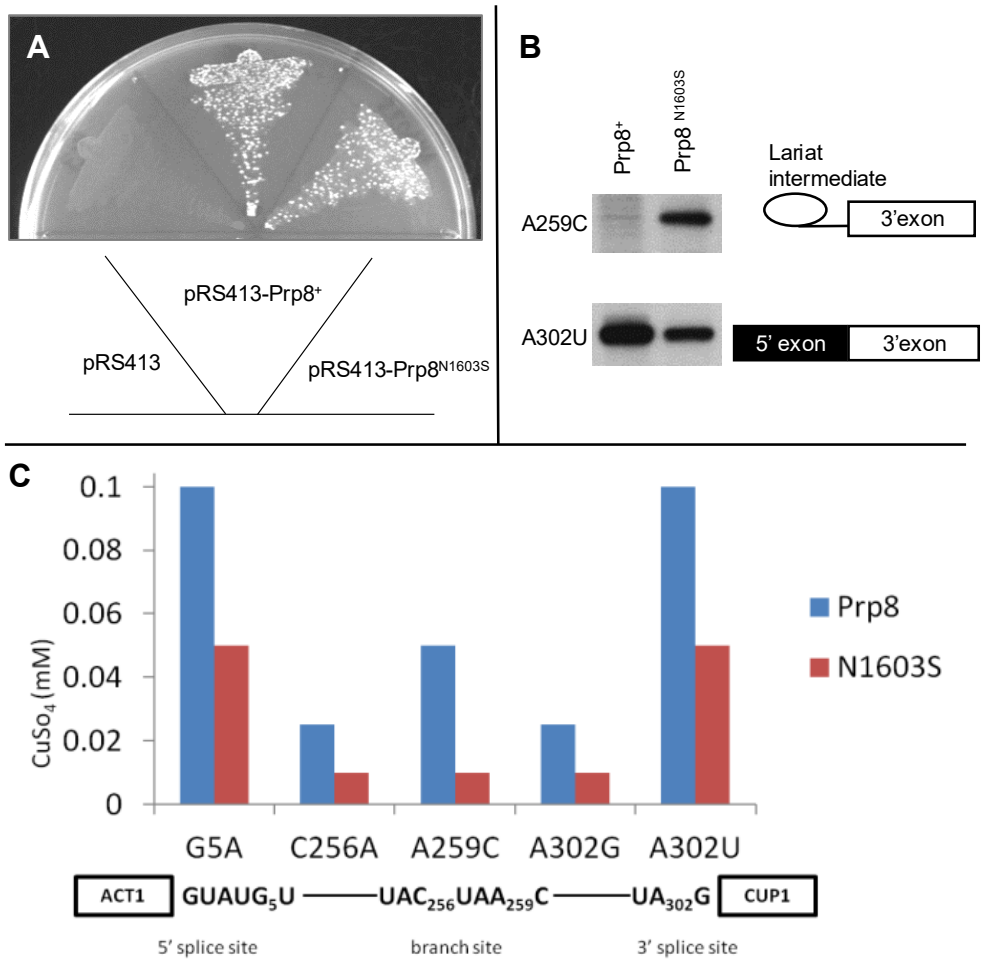

1264

1265 **Fig 5. Investigation of Prp8 N1603S substitution phenotype in yeast.** A) Growth of haploid
1266 yeast strains with genomic *PRP8* deletion and complementing pRS413 plasmids with either no
1267 PRP8, PRP8 wild-type (PRP8*) or PRP8 N1603S. Left sector: Strains transformed with empty
1268 pRS413 fail to grow, confirming genomic *PRP8* deletion is non-viable; middle and right
1269 sectors: yeast strains are viable when transformed with pRS413 containing either wild type or
1270 mutated (N1603S) *PRP8*. Plates were grown at 30°C. B) Primer extension analysis in Prp8 and
1271 Prp8^{N1603S} strains containing *ACT1-CUP1* reporters. Top panel displays lariat accumulation in
1272 the *ACT1-CUP1* A259C branch site reporter in the Prp8^{N1603S} strain. Bottom panel displays
1273 depletion of mature mRNA product in the *ACT1-CUP1* A302U 3'SS reporter in the Prp8^{N1603S}
1274 strain. These results are consistent with the N1603S mutation representing a first step allele of
1275 Prp8. C) Comparison of splicing efficiencies using *ACT1-CUP1* splicing reporters. More

efficient splicing of a reporter correlates with increased copper resistance and therefore growth at higher concentrations of copper sulphate ($CuSO_4$). Haploid yeast strains with *CUP1* and *PRP8* deletions with either wild type or N1603S Prp8 complementing plasmids were transformed with *ACT1-CUP1* splicing reporters containing mutations at the 5'SS (G5A), BPS (C256A and A259C) and the 3'SS (A302G and A302U) and grown on plates with increasing concentrations of $CuSO_4$; in each case Prp8 N1603S was less efficient at splicing the reporter compared to wild type Prp8. Graphs indicate the highest concentration of copper where all three replicates survived.

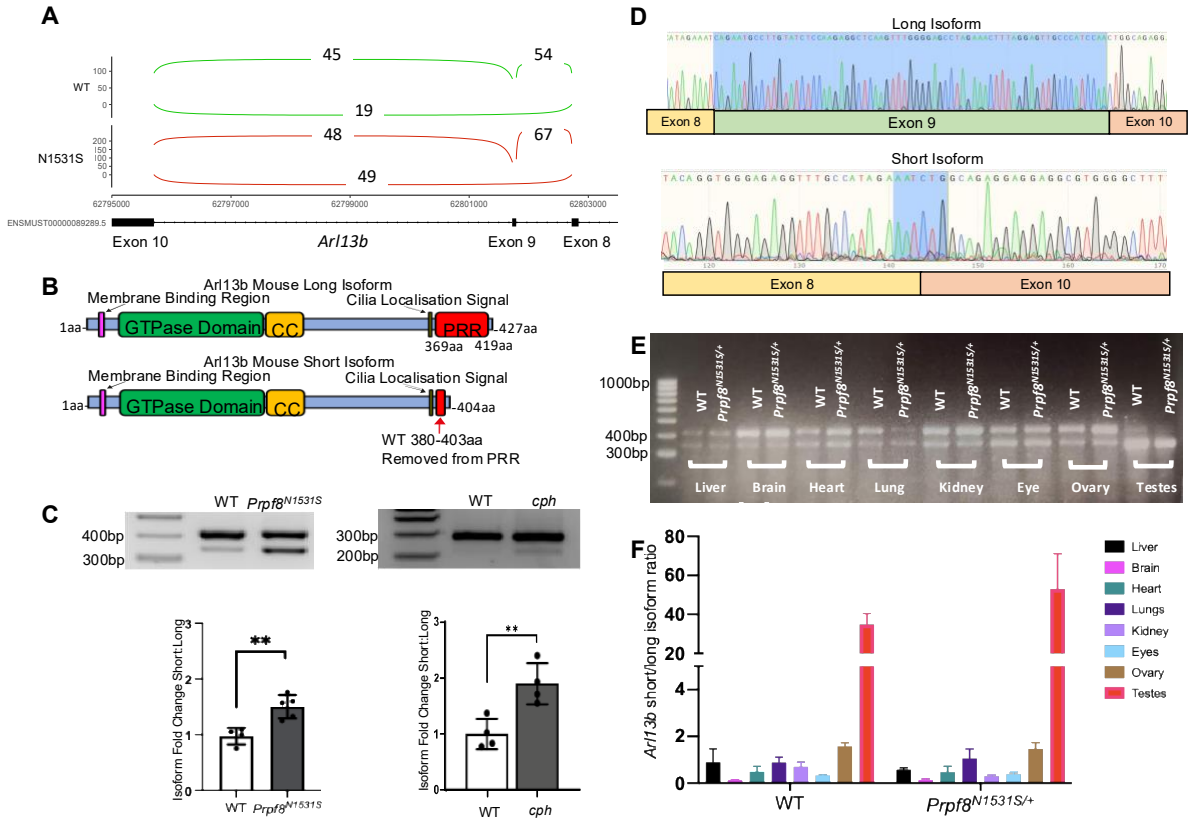

Fig 6. *Arl13b* transcript alterations present in *Prpf8* mutant mice and fish. A) Sashimi plot illustrating relative read coverage of splice junctions between exons 8 and 10 of the murine *Arl13b* transcript in three WT mice (top, green) and three *Prpf8*^{N1531S} homozygous mouse mutants (bottom, red). Numbers represent the mean read coverage across each junction for the

1290 three replicates of each genotype. *Prpf8*^{N1531S} homozygous mutants exhibit a marked increase
1291 in skipping of exon 9, producing greater levels of the *Arl13b* short isoform. B) Schematic
1292 representation of ARL13B predicted protein products found in wild type embryos and
1293 *Prpf8*^{N1531S} mouse mutants. The region of the transcript encoding amino acids 380-403 from
1294 the wild type sequence is removed from the short isoform. C) RT-PCR using a single primer
1295 pair displaying long and short isoforms of *Arl13b* in mouse (left) and zebrafish (right) embryos.
1296 Quantification of the relative proportions of the *Arl13b* short and long isoforms plotted as fold
1297 change relative to wild type are shown below the agarose gels. D) Sequencing chromatograph
1298 of *arl13b* RT-PCR product from wild type zebrafish (top) and *cph* embryos (bottom). The
1299 region corresponding to exon 9 is highlighted in the long isoform sequence. The junction
1300 between exon 8 and 10 is highlighted in the short isoform sequence. E) RT-PCR using a single
1301 primer pair displaying *Arl13b* long and short isoform distribution in wild type and *Prpf8*^{N1531S}
1302 heterozygous adult mouse organs. F) Quantification of the ratio of relative expression levels of
1303 *Arl13b* long and short isoform in wild type and *Prpf8*^{N1531S} heterozygous adult mouse organs.
1304
1305

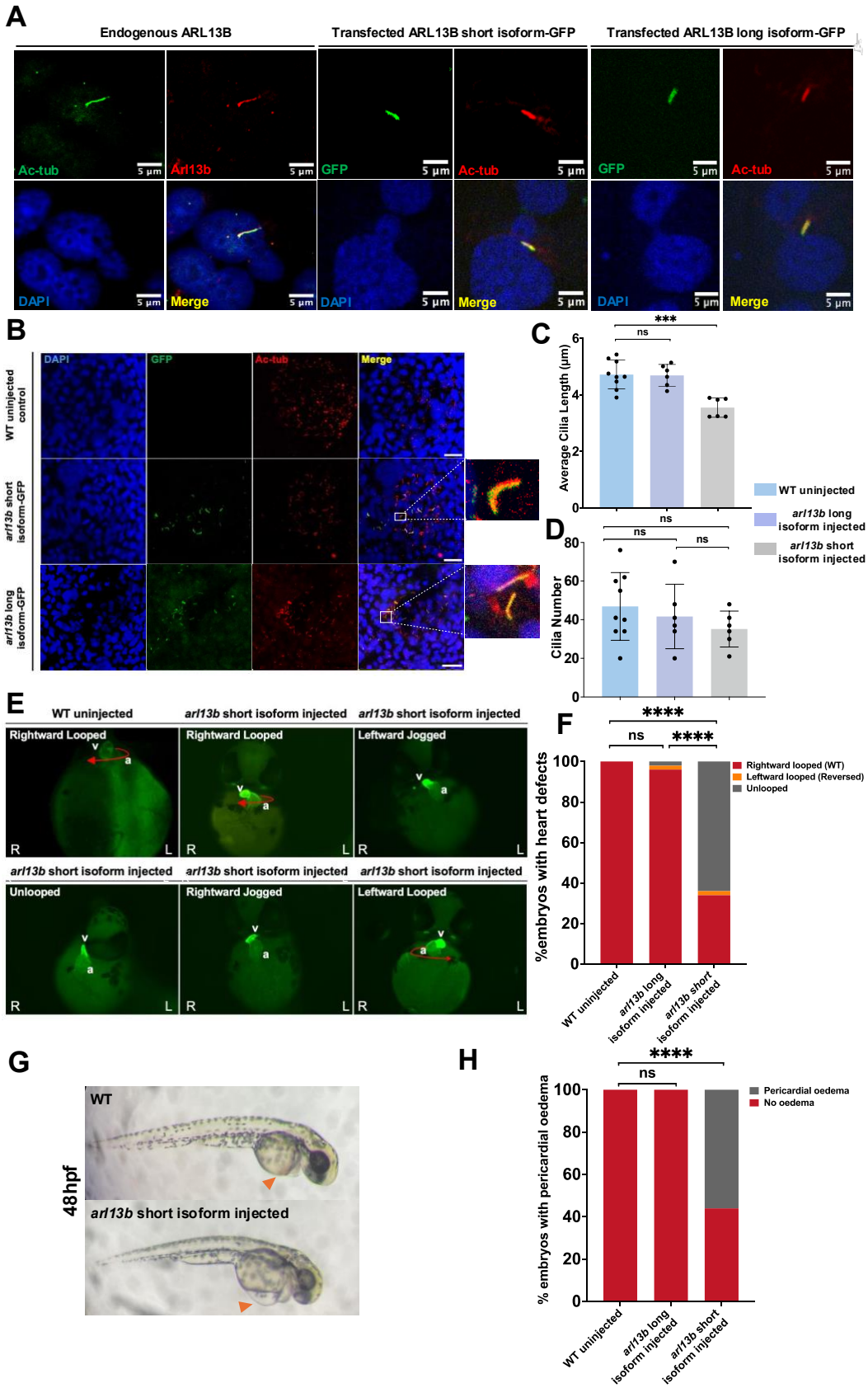

1306

1307 **Fig 7. Analysis of *ARL13B* short and long isoform over-expression in human cells and**

1308 **wild type zebrafish embryos.** A) Co-localization of human acetylated tubulin (green) and

1309 endogenous ARL13B (red; left panels); co-localization of transfected GFP-tagged human
1310 ARL13B short isoform (green) with acetylated tubulin (red; centre panels); co-localisation of
1311 transfected GFP-tagged human ARL13B long isoform (green) with acetylated tubulin (red;
1312 right panels) in hTERT-RPE1 cells. Nuclei are stained with DAPI (blue). Scale bar 5µm. B)
1313 Immunofluorescence images of KV cilia in three groups: wild type uninjected embryos (top),
1314 embryos injected with *arl13b-gfp* short isoform mRNA (middle), and embryos injected with
1315 *arl13b-gfp* long isoform mRNA (bottom). Cilia are stained with acetylated tubulin (labelling
1316 axonemes), and GFP to label the injected Arl13b protein isoforms. Nuclei are stained with
1317 DAPI. C) Quantification of average cilia length per KV in wild type uninjected control
1318 embryos (n=9); *arl13b* long isoform injected embryos (n=6), and *arl13b* short isoform
1319 injected embryos (n=6). No significant difference was detected between the *arl13b* long
1320 isoform injected embryos and the uninjected wildtype embryos (one-way ANOVA, $p > 0.05$).
1321 Cilia length in *arl13b* short isoform injected embryos was significantly decreased compared
1322 to uninjected wildtype embryos (one-way ANOVA, $p < 0.05$). Scale bar = 20µm. D)
1323 Quantification of cilia number per KV in control and injected embryos. No significant
1324 differences were detected between groups (one-way ANOVA $p > 0.05$). E) Heart
1325 directionality at 48hpf detected by MF20 immunofluorescence (red arrows). Some *arl13b*
1326 short isoform injected injected embryos show delayed cardiac development and have not
1327 achieved fully looped hearts at 48hpf, but resemble the jogging asymmetry typically present
1328 at 24hpf. Injection condition is shown above the images, observed heart directionality is
1329 shown on the images. F) A significant difference in heart defects frequency was presented
1330 among the three group (Chi-square test, $p < 0.0001$). Pairwise comparisons then were
1331 performed between groups. Embryos injected with the *arl13b* short isoform mRNA (n=50)
1332 displayed a significantly increased percentage of heart directionality defects compared with
1333 the *arl13b* long isoform mRNA injected (n=50) or wild type uninjected group (n=50)

1334 (Fisher's exact test, $p < 0.0001$), while there is no significant difference of heart defect
1335 frequency observed between the *arl13b* long isoform mRNA injected group and the wildtype
1336 uninjected group (Fisher's exact test, $p = 0.4949$) . G) Brightfield image of wild type
1337 uninjected embryo (bottom) at 48hpf lacking oedema in pericardium (orange arrowhead).
1338 *arl13b* short isoform mRNA injected embryo (bottom) at 48hpf shows pericardial oedema
1339 (orange arrowhead). H) Wild type embryos (n=50) do not display pericardial oedema at
1340 48hpf, nor do embryos injected with the *arl13b* long isoform (n=50). Embryos injected with
1341 the *arl13b* short isoform mRNA (n=50) showed a significant increase in pericardial oedema
1342 compared with the uninjected control group (Fisher's exact test, $p < 0.0001$).
1343
1344

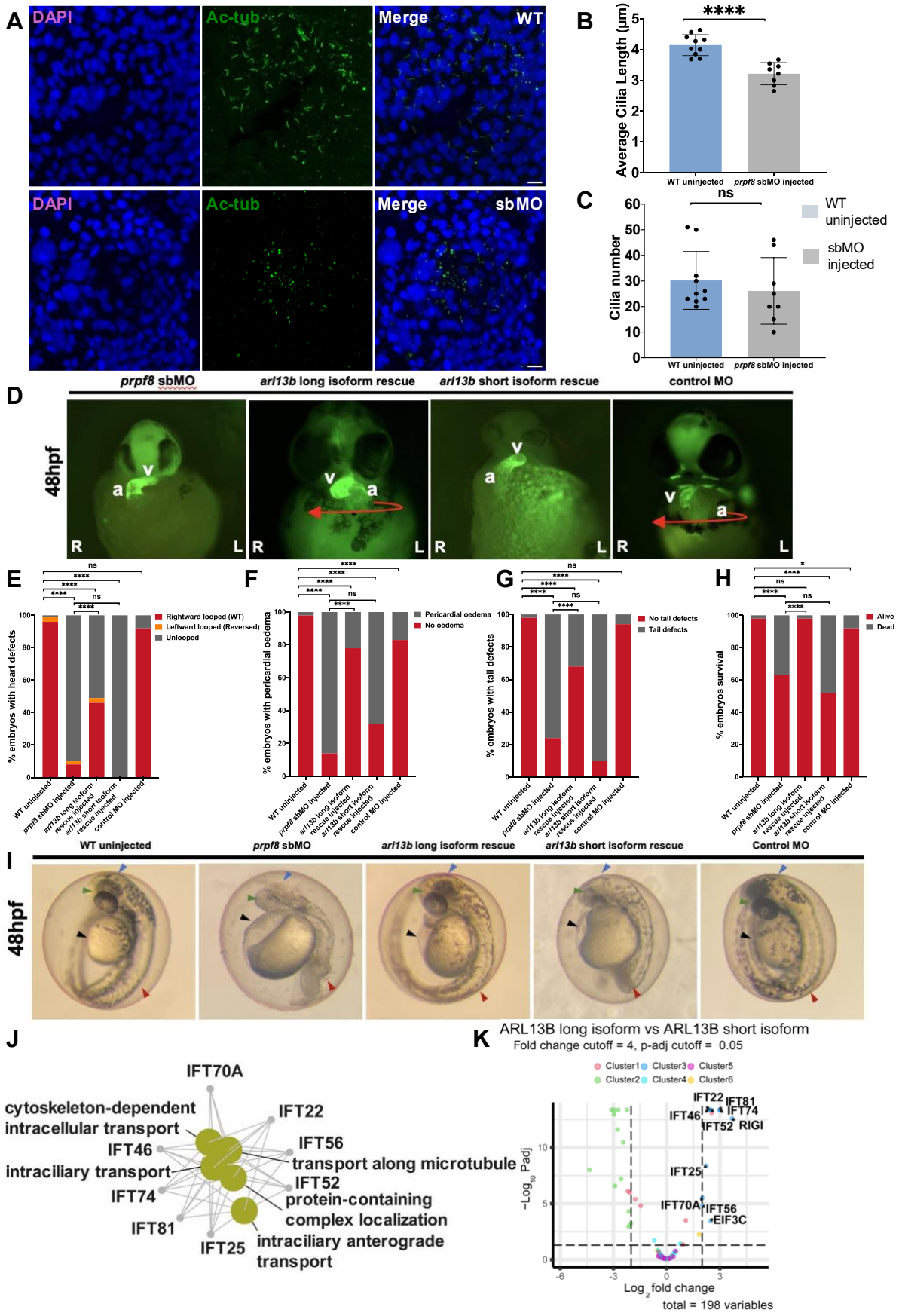
A
DAPI
Ac-tub
Merge
WT
sbMO
B
Average Cilia Length (µm)
****
WT uninjected
prpf8 sbMO injected
C
Cilia number
ns
WT uninjected
sbMO injected
prpf8 sbMO
arl13b long isoform rescue
arl13b short isoform rescue
control MO
D
48hpf
R
L
E
F
G
H
% embryos with heart defects
Rightward looped (WT)
Leftward looped (Reversed)
Unlooped
% embryos with pericardial oedema
Pericardial oedema
No oedema
% embryos with tail defects
No tail defects
Tail defects
% embryos survival
Alive
Dead
WT uninjected
prpf8 sbMO
arl13b long isoform rescue
arl13b short isoform rescue
Control MO
I
48hpf
J
IFT70A
cytoskeleton-dependent intracellular transport
IFT22
IFT46
IFT56
intraciliary transport
transport along microtubule
IFT52
IFT74
protein-containing complex localization
IFT81
IFT25
intraciliary anterograde transport
K
ARL13B long isoform vs ARL13B short isoform
Fold change cutoff = 4, p-adj cutoff = 0.05
Cluster1
Cluster2
Cluster3
Cluster4
Cluster5
Cluster6
IFT22
IFT81
IFT46
IFT74
IFT52
RIGI
IFT25
IFT70A
IFT56
EIF3C
−Log10 Padj
Log2 fold change
total = 198 variables

1345

1346 **Fig 8. Analysis of *Prpf8* sbMO knockdown phenotypes and rescue by *arl13B* long**
1347 **isoform mRNA co-injection.** A) Immunofluorescence of KV cilia stained using an antibody
1348 against acetylated tubulin labelling axonemes (green) in WT and *prpf8* sbMO knockdown
1349 embryos. Nuclei are stained with DAPI (blue). Scale bar is 10μm. B) Quantification of cilia
1350 length per KV in WT (n=10) and *prpf8* splice blocking morpholino (sbMO) knockdown
1351 embryos (n=8). All cilia detected with acetylated tubulin staining were measured, and the
1352 average length per KV is plotted. *prpf8* sbMO knockdown embryos show a significant
1353 decrease in cilia length (Unpaired t-test, $p < 0.0001$). C) Quantification of cilia number per
1354 KV showed no significant difference between groups (Unpaired t-test; $p = 0.4868$). D)
1355 Cardiac looping morphogenesis detected by MF20 immunofluorescence. sbMO embryos and
1356 *arl13b* short isoform mRNA rescue embryos showed heart looping defects. The co-injection
1357 of *arl13b* long isoform mRNA with sbMO partially rescued heart looping defects. Control
1358 MO injected embryos did not display heart directionality defects. E-H) Analysis of
1359 phenotypes in wildtype uninjected embryos (n=94), *prpf8* sbMO knockdown embryos
1360 (n=104), sbMO co-injection with *arl13b* short isoform mRNA (n=44), sbMO co-injection
1361 with *arl13b* long isoform mRNA (n=79), and control MO injected embryos (n=84).
1362 Statistical analysis was first performed using a Chi-square test to assess morphological
1363 defects among five groups. Where significant difference was observed, pairwise comparisons
1364 were conducted between two groups by Fisher's test. E) The sbMO knockdown embryos with
1365 *arl13b* long isoform mRNA injection displayed a significantly decreased percentage of heart
1366 directionality defects compared to the sbMO knockdown group (Fisher's exact test, $p <$
1367 0.0001). F) The percentage of pericardial oedema at 48hpf is significantly decreased in the
1368 *arl13b* long isoform mRNA injection rescue group compared to the sbMO knockdown group
1369 (Fisher's exact test, $p < 0.0001$). G) The percentage of tail defects is significantly decreased
1370 in the *arl13b* long isoform overexpression rescue group compared to the sbMO knockdown

1371 group (Fisher's exact test, $p < 0.0001$). H) Embryo survival at 72 hpf is significantly
1372 increased in the long isoform co-injection group compared to the sbMO knockdown group
1373 (Fisher's exact test, $p < 0.0001$). I) Brightfield images of WT embryo, *prpf8* sbMO, *arl13b*
1374 long isoform co-injected embryo, *arl13b* short isoform co-injected embryo and control MO
1375 injected embryo. Black arrowheads indicate pericardial oedema, blue arrowheads indicate
1376 head morphological defects, green arrowheads indicate eye defects, and red arrowheads
1377 indicate tail defects seen in *prpf8* sbMO injected embryos. J) Network analysis of enriched
1378 biological processes at GO Level 5 for proteins binding to the long isoform of ARL13B.
1379 Many processes related to cilia function are present. K) Volcano plot of mass spectrometry
1380 data showing proteins that are enriched for binding the long isoform of ARL13B compared to
1381 the short isoform, based on a fold-change cutoff of 4 and an adjusted p-value cutoff of 0.05.
1382 The X-axis represents the log2 fold change, and the Y-axis represents the log2 adjusted p-
1383 value. Note that many members of the IFT-B complex are significantly enriched in this
1384 comparison.
1385
1386